

1 **Bispecific Targeting of Conserved Epitopes Enables Pan-Hantavirus Neutralization**

2

3 Jiayao Yang^{1,4,10}, Zihao Jiang^{6,7,10}, Yudun Ke^{1,10}, Xuyang Zheng^{8,10}, Ziyu Liu^{9,10}, Shuliang
4 Chen^{6,7}, Lijuan Niu^{6,7}, Fan Luo^{6,7}, Ziniu Dai¹, Jinhao Bi¹, Mingxi Li¹, Xiao Dang⁸, Jiayi Shu⁵,
5 Fajie Yuan³, Zeli Zhang^{1,2}, Zhiqiang Ku^{1,2}, Ren Sun^{1,2}, Xingan Wu⁹, Jianqi Lian⁸, Rongrong
6 Liu^{9,11}, Wei Hou^{6,7,11}, Zhaoqian Wang^{1,2,11}, Dapeng Li^{1,2,11}

7

8 ¹Center for Infectious Disease Research, Zhejiang Key Laboratory of Multi-Omics in
9 Infection and Immunity, School of Medicine; ²School of Life Sciences; ³School of
10 Engineering,

11 Westlake University, Hangzhou, Zhejiang 310024, China.

12 ⁴School of Life Sciences, ⁵Clinical Center for Biotherapy, Zhongshan Hospital & Zhongshan
13 Hospital (Xiamen), Fudan University, Shanghai, China.

14 ⁶State Key Laboratory of Virology and Biosafety, Hubei Province Key Laboratory of Allergy
15 and Immunology, Institute of Medical Virology, Taikang Medical School (School of Basic
16 Medical Sciences), Wuhan University, Wuhan, Hubei 430071, China.

17 ⁷Shenzhen Research Institute, Wuhan University, Shenzhen, Guangdong 518057, China.

18 ⁸Department of Infectious Diseases, Tangdu Hospital; ⁹Department of Microbiology, School
19 of Basic Medicine, Fourth Military Medical University, Xi'an, Shaanxi 710038, China.

20 ¹⁰Co-first Authors

21 ¹¹Corresponding Authors

22

23 Correspondence: Rongrong Liu (liurongrong@fmmu.edu.cn), Wei Hou

24 (houwei@whu.edu.cn), Zhaoqian Wang (wangzhaoqian@westlake.edu.cn) and Dapeng Li

25 (lidapeng@westlake.edu.cn)

26

27 **ABSTRACT**

28 Hantaviruses cause renal and cardiopulmonary syndromes with case-fatality rates up to
29 40%, yet no approved antiviral therapy exists. Antigenic divergence between Old World and
30 New World hantaviruses has impeded the development of broadly protective antibody
31 therapeutics. Here, we isolated neutralizing antibodies from convalescent donors and
32 identified two lead antibodies targeting distinct conserved epitopes. XA-3H12 potently
33 neutralizes Old World hantaviruses, whereas XA-044 broadly neutralizes HTNV, SNV and
34 ANDV. Cryo-EM structures revealed that XA-044 recognizes the apical Gn-Gc interface,
35 whereas XA-3H12 binds the basal region of Gc domain II, defining two non-overlapping
36 conserved neutralization sites. Guided by these structures, we engineered a bispecific IgG-
37 scFv that integrates the breadth and potency of both parental antibodies and achieves broad
38 hantavirus neutralization. In mouse models, the IgG-scFv blocked entry of diverse hantavirus
39 pseudoviruses *in vivo* and conferred post-exposure protection against lethal HTNV challenge,
40 establishing a dual-epitope bispecific antibody candidate for broad hantavirus intervention.

41 INTRODUCTION

42 Hantaviruses are enveloped, segmented, negative-sense RNA viruses of the order
43 *Bunyavirales*, broadly classified into Old World and New World lineages according to their
44 geographic distribution and associated disease manifestations¹⁻³. Old World hantaviruses
45 (OWH), including Hantaan virus (HTNV), Seoul virus (SEOV), Puumala virus (PUUV), and
46 Dobrava-Belgrade virus (DOBV), circulate predominantly in Europe and Asia and cause
47 hemorrhagic fever with renal syndrome (HFRS), with case-fatality rates ranging from 1% to
48 15%⁴⁻⁶. In contrast, New World hantaviruses (NWH), such as Andes virus (ANDV) and Sin
49 Nombre virus (SNV), are endemic to the Americas and cause hantavirus cardiopulmonary
50 syndrome (HCPS), a severe respiratory disease with fatality rates approaching 40%^{4,7,8}.
51 Rodents serve as the natural reservoirs, and human infection occurs primarily through
52 inhalation of aerosolized virus-contaminated excreta⁹. Despite the substantial morbidity and
53 mortality associated with hantavirus infections, no FDA-approved antiviral therapies are
54 currently available^{6,10}. Clinical management remains largely supportive, underscoring the
55 urgent need for effective prophylactic and therapeutic countermeasures.

56 The hantavirus genome comprises three segments—small (S), medium (M), and large
57 (L)—which encode the nucleocapsid protein (NP), the glycoprotein precursor (GPC), and the
58 RNA-dependent RNA polymerase (RdRp), respectively¹¹. The GPC is processed by host
59 signal peptidase into two surface glycoproteins, Gn and Gc, which assemble into tetrameric,
60 square-shaped (Gn/Gc)₄ on the virion surface^{12,13}. These glycoproteins mediate viral
61 attachment, endosomal entry, and membrane fusion, and constitute the principal targets of the
62 host neutralizing antibody response¹⁴⁻¹⁹. Accordingly, Gn and Gc represent the most attractive
63 antigens for vaccine design and antibody-based therapeutic development.

64 Although antibody-based countermeasures hold considerable promise, developing a
65 broadly protective therapeutic capable of addressing the extensive antigenic diversity of
66 hantaviruses remains a major challenge. Previously identified monoclonal antibodies have
67 demonstrated encouraging activity, but important gaps remain. For example, neutralizing
68 antibodies isolated from convalescent donors protected against NWH, yet their neutralizing
69 capacity against major HFRS-causing viruses such as HTNV and SEOV was not defined, and
70 the lack of epitope mapping limited mechanistic understanding^{3,18}. More recently, the broadly

71 neutralizing antibody ADI-42898, isolated from a PUUV-infected individual^{20,21}, representing
72 an important conceptual advance for the development of pan-hantavirus antibody
73 countermeasures. However, ADI-42898 showed relatively limited neutralizing potency
74 against several clinically important hantaviruses, including HTNV, and its activity relies on
75 recognition of a single conserved epitope. Thus, antibody-based therapeutics that achieve
76 broad-spectrum neutralization by simultaneously targeting two distinct conserved epitopes—
77 and thereby may reduce the likelihood of viral escape—remain an important unmet need.

78 Here, we address this gap by isolating and characterizing a panel of potent neutralizing
79 antibodies from four HFRS convalescent donors. From this panel, we identified two lead
80 antibodies with distinct neutralization profiles: XA-3H12, a highly potent neutralizer of the
81 OWHs HTNV and SEOV, and XA-044, a broadly reactive antibody that neutralizes HTNV as
82 well as the NWHs SNV and ANDV. Cryo-EM analyses revealed that these antibodies
83 recognize two non-overlapping conserved epitopes on the hantavirus Gn-Gc glycoprotein
84 complex, providing a structural basis for their neutralizing activities. Guided by these
85 findings, we evaluated multiple bispecific antibody formats and identified an IgG-scFv
86 derivative with the strongest breadth and potency. This bispecific antibody achieved broad-
87 spectrum neutralization across OWHs and NWHs, blocked viral entry *in vivo* in a
88 bioluminescent vesicular stomatitis virus (VSV)-pseudotyped hantavirus reporter system, and
89 provided robust post-exposure protection in a lethal HTNV mouse challenge model. Together,
90 these findings establish a dual-epitope bispecific antibody as a promising pan-hantavirus
91 therapeutic candidate and provide structural guidance for the rational design of next-
92 generation hantavirus vaccines.

94 RESULTS

95 Isolation of cross-reactive antibodies from HFRS convalescent patients

96 We collected blood samples from four individuals who had recovered from HFRS.
97 Plasma from all four donors showed strong binding to HTNV and SEOV Gn and Gc antigens
98 (*Extended Data Fig. 1a,b*). To assess cross-reactive neutralizing activity against both OWH
99 and NWH, we used recombinant VSV pseudoviruses (rVSV) bearing the Gn-Gc
100 glycoproteins of HTNV, SEOV, SNV, and ANDV^{22,23}. Donor plasma exhibited broad and

101 potent neutralization of OWH pseudoviruses, whereas neutralization of NWH pseudoviruses
102 was variable but detectable (**Fig. 1a**).

103 To isolate antigen-specific memory B cells, peripheral blood mononuclear cells
104 (PBMCs) were sorted using biotinylated HTNV and SEOV Gn and Gc proteins as probes,
105 followed by single-cell PCR amplification or single-cell B-cell receptor sequencing (scBCR-
106 seq) (**Fig. 1b and Extended Data Fig. 1c**). We sorted 384 Gn/Gc-specific single B cells and
107 recovered 323 paired heavy- and light-chain sequences for recombinant IgG expression. An
108 additional 68 paired sequences were selected for synthesis based on somatic hypermutation
109 (SHM) rates and complementarity-determining region 3 (CDR3) lengths. Screening of the
110 resulting recombinant antibodies against Gn and Gc from HTNV, SEOV, SNV, and ANDV
111 identified 117 antibodies reactive with at least one virus (**Extended Data Table 1**). The mean
112 SHM rates of the heavy and light chains were 7.9% and 5.3%, respectively (**Fig. 1c**), and the
113 mean CDR3 lengths were 18 and 10 amino acids, respectively (**Fig. 1d**). Among these
114 antibodies, 9 Gn-directed and 21 Gc-directed antibodies displayed cross-reactivity across
115 multiple viruses. Gn cross-reactive antibodies were largely restricted to OWH, whereas Gc-
116 directed antibodies exhibited broader reactivity, including strong binding to NWH Gc (**Fig.**
117 **1e**). Collectively, these data demonstrate that cross-reactive antibodies targeting diverse
118 hantaviruses exist in HFERS convalescent donors.

119

120 **Identification of NAbs targeting distinct hantavirus Gn/Gc neutralization sites**

121 We next screened Gn/Gc-specific antibodies for binding to the Gn head domain and Gc
122 ectodomain (**Fig. 2a**), and for neutralizing activity against rVSV-HTNV (**Extended Data**
123 **Table 1**). Fifteen NAbs, including 10 derived from single-cell PCR and 5 from scBCR-seq,
124 were selected for further characterization (**Extended Data Fig. 2a**). Binding was assessed
125 against isolated Gn head, Gc ectodomain, and a heterodimeric Gn^HGc construct that
126 recapitulates the native quaternary architecture of hantavirus glycoproteins (**Fig. 2b**)¹². Most
127 antibodies preferentially recognized OWH antigens, with limited binding to NWH
128 glycoproteins (**Fig. 2c and Extended Data Fig. 2b, c**). Several antibodies, including XA-1A5,
129 XA-1D4, XA-044, and XA-060, bound weakly to isolated Gn or Gc but recognized Gn^HGc,

130 indicating conformation-dependent epitopes. Notably, XA-044 was the only antibody that
131 strongly bound NWH Gn^HGc, recognizing HTNV, SNV, and ANDV, but not SEOV.

132 Neutralization assays against OWH and NWH pseudoviruses showed that 12 antibodies
133 potently neutralized rVSV-HTNV, with IC₅₀ values below 0.01 µg/mL, whereas three showed
134 moderate activity. Five antibodies—XA-3A8, XA-3H12, XA-4E4, XA-4G11, and XA-058—
135 cross-neutralized rVSV-HTNV and rVSV-SEOV (*Fig. 2d and Extended Data Fig. 2d*).
136 Consistent with its binding profile, XA-044 potently neutralized HTNV, SNV, and ANDV
137 pseudoviruses, but not SEOV. Five antibodies also neutralized authentic HTNV, among
138 which XA-3H12 and XA-044 were the most potent, with IC₅₀ values of 0.034 and 0.013
139 µg/mL, respectively (*Fig. 2d and Extended Data Fig. 2e*).

140 To map the antigenic landscape, we performed Biolayer Interferometry (BLI)-based
141 competition assays using HTNV glycoproteins. The 15 NAbs segregated into five antigenic
142 sites, A1, A2, B, C, and D (*Fig. 2e and Extended Data Fig. 3*). Site A1, targeted by XA-044,
143 represented a conserved epitope shared by HTNV, SNV, and ANDV, whereas site C targeted
144 by XA-3H12 defined a major OWH neutralizing site. Sites B and D were primarily associated
145 with OWH Gn- and Gc-directed antibodies, respectively. These data reveal multiple
146 neutralizing vulnerabilities on hantavirus Gn^HGc with distinct breadth profiles.

147

148 **Structural basis of broad neutralization by XA-044 and XA-3H12**

149 Having identified XA-044 and XA-3H12 as two of the most potent NAbs targeting
150 distinct antigenic sites with complementary breadth profiles—site A1 and site C,
151 respectively—we next sought to define the structural basis of their recognition and
152 neutralization. We therefore determined the structures of XA-044 Fab bound to SNV Gn^HGc
153 and XA-3H12 Fab bound to HTNV Gn^HGc (*Extended Data Table 2*). Superposition onto the
154 ANDV Gn-Gc dimer (PDB: 9P3X)¹³ showed that XA-044 targets the apical Gn-Gc interface,
155 whereas XA-3H12 binds the basal region of Gc domain II (*Fig. 3a*). XA-044 buries >720 Å²
156 of surface area through shape complementarity and seven hydrogen bonds, using CDR L1-2
157 and H3 to contact SNV Gn residues 73-79 and Gc residues 90-92, 129-130, 91-93, 110-115,
158 129 and 131 (*Fig. 3b,d*). Its epitope partially overlaps that of ADI-65534^{13,21}, but is shifted
159 toward the Gc fusion-loop region while retaining Gn capping-loop contacts (*Extended Data*

160 **Fig. 4a**). In contrast, XA-3H12 buries $>1025 \text{ \AA}^2$ on HTNV Gc alone through shape
161 complementarity, hydrogen bonds and salt bridges mediated by CDR L1, L3, H1-3 and FR3,
162 contacting residues 67-72, 147-150, 152, 194-195, 216-219, 225-238 (except 227 and 229),
163 and 288-289; the heavy chain forms eight hydrogen bonds and two salt bridges, and the light
164 chain forms three hydrogen bonds (**Fig. 3e,g**). Notably, N-glycosylation protruded from N328
165 of HTNV Gn may also stabilize XA-3H12 binding (**Extended Data Fig. 4b**).

166 Conservation analysis showed that 9/13 XA-044 epitope residues on SNV Gc are fully
167 conserved and 13/13 are $>70\%$ conserved across OWHs and NWHs, whereas 6/7 Gn residues
168 are $>50\%$ conserved; for XA-3H12, 10/31 epitope residues on HTNV Gc are fully conserved
169 and 25/31 are $>50\%$ conserved (**Fig. 3h,i**). Structural superposition onto the ANDV Gn-Gc
170 tetramer (PDB: 9P3Y)¹³ revealed no clash within a single tetramer, but in the tetramer-dimer
171 interface XA-044 shows minor or no clash with neighboring Gc, whereas XA-3H12 exhibits a
172 major clash with neighboring Gn (**Fig. 3j and Extended Data Fig. 4c,d**). Together, these
173 structures identify two spatially distinct and conserved neutralizing epitopes on the hantavirus
174 Gn-Gc complex that underlie the complementary neutralization profiles of XA-044 and XA-
175 3H12. The non-overlapping binding modes, together with their distinct breadth and potency,
176 provided a structural rationale for combining these antibodies and for engineering bispecific
177 formats capable of simultaneously engaging both neutralizing sites.

178

179 **Bispecific antibody strategies achieve pan-hantavirus neutralization**

180 Guided by the structural demonstration that XA-044 and XA-3H12 recognize spatially
181 distinct and conserved neutralizing epitopes, and by their complementary neutralization
182 breadth, we next asked whether co-targeting these two sites could enhance potency and
183 expand hantavirus coverage. We therefore performed BLI analyses to characterize the binding
184 profiles of XA-044 and XA-3H12 against representative OWH and NWH Gn^HGc antigens.
185 XA-3H12 bound HTNV, SEOV, and SNV Gn^HGc with picomolar to subpicomolar affinities,
186 whereas XA-044 bound ANDV Gn^HGc with subpicomolar affinity ($K_D < 1 \text{ pM}$) and also
187 showed high-affinity binding to HTNV and SNV Gn^HGc, but not SEOV (**Fig. 4a and**
188 **Extended Data Fig. 5a**). Consistent with the structural analysis, BLI-based competition
189 assays confirmed that XA-044 and XA-3H12 can simultaneously engage Gn^HGc without

190 detectable competition, supporting their combined use (**Fig. 4b**). We next assessed whether
191 these two antibodies act synergistically in neutralization. In a checkerboard assay spanning
192 concentrations around their individual IC₅₀ values, the XA-044/XA-3H12 cocktail achieved
193 91.67% neutralization at the combined IC₅₀ concentration, exceeding the 75% expected from
194 simple additivity (**Fig. 4c**). These results indicate that co-targeting both neutralization sites
195 produces synergistic enhancement of neutralization potency.

196 To identify an optimal combinatorial format, we evaluated five designs: a two-antibody
197 cocktail, Knob-into-Hole, CrossMab, Fab-scFv, and IgG-scFv. All formats potently
198 neutralized HTNV, with the cocktail, Fab-scFv, and IgG-scFv achieving IC₅₀ values below 1
199 ng/mL (**Fig. 4d and Extended Data Fig. 5b**). However, Knob-into-Hole, CrossMab, and Fab-
200 scFv showed reduced activity against NWH pseudoviruses, including SNV, ANDV, JUQV,
201 and LNV. By contrast, the cocktail and IgG-scFv preserved the breadth and potency of both
202 parental antibodies, with IC₅₀ values comparable to those of XA-044 or XA-3H12 alone (**Fig.**
203 **4d and Extended Data Fig. 5b**). Consistently, cell-surface staining of cells expressing full-
204 length viral glycoproteins showed that IgG-scFv combined the binding breadth of both
205 parental antibodies. Whereas XA-3H12 and XA-044 each displayed more restricted binding
206 profiles, IgG-scFv recognized all tested viruses bound by either antibody, including the
207 OWHs HTNV, SEOV, DOBV, and PUUV, as well as the NWHs SNV, ANDV, LNV, JUQV,
208 and CHOV (**Fig. 4e,f and Extended Data Fig. 5c**). Together, these *in vitro* binding and
209 neutralization data demonstrate that the structurally guided IgG-scFv design successfully
210 integrates the complementary breadth and potency of XA-044 and XA-3H12 into a single
211 bispecific molecule. Thus, we advanced the IgG-scFv for subsequent *in vivo* evaluation, with
212 the parental-antibody cocktail included as a benchmark comparator.

213

214 **A pseudovirus reporter system enables *in vivo* evaluation of hantavirus entry blockade**

215 To evaluate hantavirus NAbs *in vivo* under Animal Biosafety Level (ABSL)-2
216 conditions, we generated four luciferase-expressing hantavirus pseudoviruses: rVSV-HTNV-
217 Luc, rVSV-SEOV-Luc, rVSV-SNV-Luc, and rVSV-ANDV-Luc (**Fig. 5a**). After
218 intraperitoneal injection into BALB/c mice, bioluminescence imaging over 9 hours showed
219 that luciferase signals became detectable at 2 hours post-infection, increased progressively

220 from 2 to 6 hours, and then plateaued between 6 and 9 hours (**Fig. 5b and Extended Data**
221 **Fig. 6a**). Three-dimensional optical tomography (**Fig. 5c and Extended Data Fig. 6b**) and
222 immunohistochemistry (**Fig. 5d and Extended Data Fig. 6c**) further identified the lungs and
223 intestines as the principal sites of pseudovirus accumulation. These results establish an
224 ABSL-2-compatible *in vivo* reporter platform for tracking hantavirus pseudovirus entry and
225 define a suitable time window for assessing antibody-mediated entry blockade.

226 To validate this system, pseudoviruses were pre-incubated with antibodies for 1 hour at
227 37°C before intraperitoneal administration (**Fig. 5e**). At 6 hours post-infection, mice receiving
228 isotype control antibody showed robust bioluminescence, whereas treatment with XA-3H12,
229 XA-044, the XA-3H12/XA-044 cocktail, or IgG-scFv markedly reduced HTNV pseudovirus
230 signals (**Fig. 5f and Extended Data Fig. 7a**). For SEOV pseudovirus, efficient entry blockade
231 was observed with XA-3H12, the cocktail, and IgG-scFv, whereas XA-044 alone showed
232 limited activity (**Fig. 5g and Extended Data Fig. 7a**). Conversely, XA-044, the cocktail, and
233 IgG-scFv potently inhibited SNV and ANDV pseudovirus entry, while XA-3H12 alone was
234 ineffective (**Fig. 5h,i and Extended Data Fig. 7a**). Thus, the *in vivo* entry-blockade profiles
235 closely matched the *in vitro* neutralization breadth of each antibody, validating this
236 pseudovirus reporter system as a robust platform for evaluating hantavirus NAbs *in vivo*.

237

238 **Bispecific strategies confer broad hantavirus entry blockade *in vivo***

239 To evaluate the prophylactic efficacy of these antibodies *in vivo*, we administered
240 individual mAbs, the XA-044/XA-3H12 cocktail, or the bispecific IgG-scFv intraperitoneally
241 to BALB/c mice 18 hours before challenge with luciferase-expressing hantavirus
242 pseudoviruses. Viral entry was assessed by bioluminescence imaging 6 hours after
243 pseudovirus challenge (**Fig. 6a**). Compared with isotype-control-treated mice, all antibody-
244 treated groups showed markedly reduced HTNV pseudovirus signals, indicating effective
245 blockade of HTNV entry by XA-044, XA-3H12, the cocktail, and IgG-scFv (**Fig. 6b and**
246 **Extended Data Fig. 7b**). Consistent with their *in vitro* neutralization profiles and the pre-
247 incubation blockade results, XA-044 conferred limited protection against SEOV pseudovirus,
248 whereas XA-3H12 failed to protect against SNV and ANDV pseudoviruses. In contrast, mice
249 pre-treated with either the XA-044/XA-3H12 cocktail or IgG-scFv exhibited markedly

250 reduced luminescence across all four pseudovirus challenges (**Fig. 6b,e and Extended Data**
251 **Fig. 7b**). These results demonstrate that both the antibody cocktail and the bispecific IgG-
252 scFv provide broad prophylactic protection against entry of diverse hantavirus pseudoviruses,
253 spanning both OWHs and NWHs.

254

255 **Post-exposure antibody therapy protects mice from lethal HTNV challenge**

256 We next evaluated the therapeutic efficacy of the XA-044/XA-3H12 cocktail and the
257 bispecific IgG-scFv in a lethal authentic HTNV infection model in suckling mice. Given the
258 clinical relevance of post-exposure intervention, antibodies were administered 24 h after
259 HTNV challenge (**Fig. 6f**). In the isotype-control group, mortality began on day 15, and all
260 animals succumbed to infection by day 18 post-infection. By contrast, both the XA-044/XA-
261 3H12 cocktail and the bispecific IgG-scFv conferred substantial protection, with only 1 and 2
262 deaths observed in the cocktail- and IgG-scFv-treated groups, respectively (**Fig. 6g**).

263 Consistent with these survival outcomes, isotype-control-treated mice exhibited weight
264 stagnation or loss beginning around day 14 post-infection, whereas antibody-treated mice
265 continued to gain weight throughout the observation period (**Fig. 6g**). Quantification of viral
266 RNA by qRT-PCR at the endpoint further showed that HTNV RNA was undetectable or
267 markedly reduced in the brain, lungs, spleen, and kidneys of antibody-treated mice, indicating
268 that post-exposure antibody administration effectively restricted systemic viral dissemination
269 (**Fig. 6h**). Collectively, these findings demonstrate that both the XA-044/XA-3H12 cocktail
270 and the bispecific IgG-scFv provide potent post-exposure protection against lethal HTNV
271 infection *in vivo*.

272

273 **DISCUSSION**

274 Hantaviruses remain a persistent and significant zoonotic threat, as illustrated by the
275 recent Andes virus outbreak linked to a South American cruise ship²⁴. Their broad rodent
276 reservoirs, recurrent spillover, and—in the case of Andes virus—capacity for human-to-
277 human transmission underscore the need for countermeasures that can protect against diverse
278 hantaviruses, including those that may emerge in future outbreaks. However, no approved
279 specific therapeutics or broadly protective vaccines are currently available. Antibody

280 development has been constrained by the antigenic diversity of the Gn-Gc glycoprotein
281 complex, with most neutralizing antibodies exhibiting either lineage-restricted activity or
282 limited broad-spectrum potency when targeting a single epitope. In this study, we establish a
283 dual-epitope bispecific strategy to overcome these limitations and broaden hantavirus
284 antibody coverage. By simultaneously engaging two distinct conserved neutralization sites
285 recognized by XA-044 and XA-3H12 within an IgG-scFv architecture, we achieve broad
286 neutralization against representative OWHs and NWHs, conferring robust *in vivo* protection
287 across diverse pseudovirus and lethal HTNV challenge models.

288 Cryo-EM structures reveal the basis of broad neutralization against both OWHs and
289 NWHs. XA-044 recognizes a conserved epitope at the apical Gn-Gc interface, with key
290 contacts extending into the Gc fusion-loop region ¹². Although this epitope includes a
291 relatively less conserved Gn capping loop, its broader footprint on the highly conserved apical
292 Gc surface likely underlies the breadth of XA-044, and suggests a mechanism of fusion
293 blockade similar to that proposed for ADI-65534 and ADI-42898 ^{13,21}. XA-3H12, in contrast,
294 binds the basal region of Gc domain II and likely disrupts Gn-Gc lattice assembly on the
295 virion surface. Thus, XA-044 and XA-3H12 define two spatially separated but conserved
296 vulnerabilities on the hantavirus glycoprotein complex.

297 The structural and functional data support a combinatorial strategy for achieving broad-
298 spectrum hantavirus protection. Although individual antibodies with cross-reactive activity
299 have been described ^{20,21}, the antigenic divergence between OWHs and NWHs makes it
300 difficult for a single specificity to combine maximal potency and breadth. In this context, XA-
301 044 and XA-3H12 provide a rational two-antibody solution. Competition-binding
302 experiments demonstrated that the two antibodies recognize non-overlapping epitopes on the
303 Gn-Gc complex and can bind antigen simultaneously, while neutralization assays showed that
304 their combined use produces synergistic activity. These findings provide a mechanistic
305 rationale for dual targeting: simultaneous engagement of two conserved neutralizing sites can
306 expand broad-spectrum coverage while potentially increasing the genetic barrier to escape. To
307 translate this concept into a single-molecule format, we evaluated five bispecific antibody
308 designs and found that only the IgG-scFv format matched or exceeded the cocktail. A
309 plausible explanation is architectural: the longer and more flexible IgG-scFv format may

310 better accommodate the distance between the XA-044 and XA-3H12 epitopes, allowing
311 simultaneous engagement on the same virion or neighboring glycoprotein complexes. By
312 contrast, more compact formats, including knob-into-hole, CrossMab, and Fab-scFv, may
313 position the two binding arms too closely or impose geometric constraints that limit
314 productive dual engagement. Importantly, with efficacy comparable to the cocktail *in vitro*
315 and *in vivo*, the IgG-scFv format offers practical advantages as a single therapeutic product,
316 including simplified manufacturing, release testing, dosing, and clinical development relative
317 to a two-component cocktail. More broadly, bispecific targeting of two conserved but distinct
318 epitopes may provide a generalizable strategy for developing antibody countermeasures
319 against antigenically diverse bunyaviruses.

320 A major practical barrier in hantavirus countermeasure development is the restricted
321 access, high cost and low throughput of authentic-virus studies under high-containment
322 conditions. For instance, HTNV and SEOV generally require ABSL-3, whereas highly
323 pathogenic NWHs such as ANDV and SNV require ABSL-4. To address this limitation, we
324 established a ABSL-2-compatible bioluminescent pseudovirus challenge model bearing
325 hantavirus Gn-Gc glycoproteins, enabling rapid and quantitative *in vivo* assessment of
326 neutralizing antibodies across multiple hantaviruses. The concordance between this model
327 and the authentic HTNV lethal challenge—both identifying the cocktail and IgG-scFv as
328 protective and revealing the limitations of individual antibodies—supports its utility as a
329 preclinical prioritization tool. Although this system cannot fully replace authentic-virus
330 protection studies, it can serve as an efficient prescreening step to prioritize candidates before
331 costly and labor-intensive high-containment experiments. This platform should also facilitate
332 evaluation of both passive antibody-based protection and active vaccine-induced neutralizing
333 responses against panels of antigenically diverse hantaviruses.

334 This study has several limitations. First, although protection against authentic HTNV
335 was demonstrated, live-virus validation against BSL-4-restricted ANDV and SNV remains
336 essential but was beyond the scope of the present study due to containment and strain-access
337 limitations. Second, further studies using serial passage or deep mutational scanning will be
338 needed to define potential escape mutations for both the antibody cocktail and the IgG-scFv
339 bispecific antibody. Third, the *in vivo* pseudovirus model does not capture post-entry steps of

340 viral replication, pathogenesis, or Fc-mediated antibody functions. Finally, the neonatal
341 mouse HTNV challenge model does not fully recapitulate adult immunity or human
342 hantavirus disease, therefore the 24 h post-exposure efficacy observed in this model has
343 limited clinical relevance; the therapeutic window, optimal dosing, and durability of
344 protection should be further evaluated in more disease-relevant models, such as non-human
345 primates. Nonetheless, the ability of XA-044 and XA-3H12 to simultaneously target two
346 conserved sites of vulnerability on the Gn-Gc complex supports a dual-specificity strategy for
347 both antibody therapy and rational pan-hantavirus vaccine design.

348

349 **METHODS**

350 **Human subjects and PBMC isolation**

351 Convalescent blood samples were collected from four HFRS donors admitted by Tangdu
352 hospital in 2023-2024. PBMCs and matched plasma samples were obtained from
353 convalescent patients more than 6 months after discharge. The participants gave written
354 informed consent to participate in this study. This study was approved by the Ethics Review
355 Committee of Tangdu Hospital (IEC of Institution for National Drug Clinical Trials, Tangdu
356 Hospital, Fourth Military Medical University, approval # 202409-14 and K202410-35) and
357 Ethics Review Committee of Westlake University (approval # 20240423LDP001).

358 Peripheral blood samples were obtained from donors in EDTA-coated collection tubes
359 and processed immediately for PBMC isolation using lymphocyte separation tubes
360 (DAKEWE, Cat # 7922112). Blood samples were centrifuged at $400 \times g$ for 20 min to
361 separate plasma and cellular components. The plasma fraction was harvested and preserved at
362 $-80\text{ }^{\circ}\text{C}$ for subsequent analyses. The remaining blood cells were diluted with an equal volume
363 of D-PBS (Servicebio, Cat # G4200) and subjected to density-gradient centrifugation.
364 Mononuclear cells enriched at the interphase were carefully collected and stored at $-80\text{ }^{\circ}\text{C}$
365 until further use.

366

367 **Recombinant Protein Expression, Purification, and Biotinylation**

368 Codon-optimized sequences encoding the Gn head domain (1,062 bp) and Gc
369 ectodomain (1,347 bp) consensus sequences of HTNV and SEOV²⁵ were individually cloned

370 into the *Drosophila* S2 expression vector pMT/BiP with a C-terminal Avi-tag and 6×His-tag.
371 The Gn head domain (1,071 bp) and Gc ectodomain (1,341 bp) sequences of SNV²⁶, and the
372 Gn head domain (1,068 bp) and Gc ectodomain (1,350 bp) sequences of ANDV²⁷ were
373 individually cloned into the *Drosophila* S2 expression vector pMT/BiP with a C-terminal
374 6×His-tag. For the generation of heterodimeric Gn^HGc constructs from HTNV, SEOV, SNV,
375 and ANDV, the Gn head domain and Gc ectodomain were linked by the amino acid sequence
376 GGSGLVPRGSGGGSGGGSWSHPQFEKGGGTGGGTLVPRGSGTGG as previously
377 described¹², and the resulting constructs were individually cloned into pMT/BiP with a C-
378 terminal 6×His-tag. Recombinant plasmids were transfected into *Drosophila* S2 cells
379 (Invitrogen, Cat # K2780-01), and stable cell lines were generated by selection with
380 blasticidin (25 µg/ml; Beyotime, Cat # ST018). Protein expression was induced with 10 µM
381 CdCl₂ (Macklin, Cat # C805627) for 5 days. Culture supernatants were collected, filtered
382 through a 0.22-µm membrane, and buffer-exchanged using a 10-kDa MWCO VIVAFLOW
383 200 module (Sartorius, Cat # VF20H0) to remove residual CdCl₂. Recombinant proteins were
384 purified by Ni²⁺ affinity chromatography (SunResin, Cat # A453201) using an ÄKTA system
385 and subsequently biotinylated through the Avi-tag using a Biotin Labeling Kit (Beyotime, Cat
386 # P0630S).

387

388 **Isolation and Sorting of Antigen-Specific B Cells**

389 B cells were enriched from PBMCs using a human pan-B cell isolation kit (BioLegend,
390 Cat # 480082) and stained with Zombie Aqua viability dye (BioLegend, Cat # 423102), anti-
391 human CD14-BV605 (BioLegend, Cat # 301834), anti-human CD16-BV785 (BioLegend, Cat
392 # 302046), anti-human CD3-PE-Cy5 (BioLegend, Cat # 300310), anti-human CD19-APC-
393 Cy7 (BioLegend, Cat # 363010), anti-human IgD-FITC (BioLegend, Cat # 348206), and anti-
394 human IgM-PerCP-Cy5.5 (BD Biosciences, Cat # 561285) for 30 min at 4 °C in the dark. To
395 identify HTNV- and SEOV-specific B cells, biotinylated Gn or Gc proteins were
396 precomplexed with PE-streptavidin (BioLegend, Cat # 405204) or APC-streptavidin
397 (BioLegend, Cat # 405207) to generate tetrameric probes, followed by incubation with
398 enriched B cells. Cells were analyzed and sorted on a CytoFLEX SRT flow cytometer
399 (Beckman Coulter). Antigen-specific B cells were defined as

400 CD14⁻CD16⁻CD3⁻CD19⁺IgM⁻IgD⁻PE⁺ or CD14⁻CD16⁻CD3⁻CD19⁺IgM⁻ IgD⁻APC⁺
401 populations.

402 For antibody gene amplification and cloning, single antigen-specific B cells were sorted
403 into 96-well PCR plates containing 20 μ L lysis buffer per well [2.5 μ L 10 \times RT buffer, 2.5 μ L
404 5 \times gDNA wiper mix (Vazyme, Cat # R312), 0.0625 μ L IGEPAL (Sigma-Aldrich, Cat #
405 I8896), 0.5 μ L carrier RNA (Sangon Biotech, Cat # B518271-0100), and 14.4375 μ L
406 nuclease-free water]. Plates were briefly centrifuged and stored at -80°C until use. For
407 single-cell transcriptome and BCR sequencing, antigen-specific B cells were sorted into D-
408 PBS containing 2% FBS, counted, and processed for downstream sequencing analyses.

409

410 **Single B Cell PCR**

411 Single B-cell antibody gene amplification and cloning were performed as previously
412 described²⁸. Briefly, cDNA was synthesized from individually sorted B cells using the
413 HiScript III First-Strand cDNA Synthesis Kit (Vazyme, Cat # R312). Immunoglobulin heavy-
414 chain (HC) and light-chain (LC) variable regions were amplified by two rounds of PCR. The
415 first round used primers targeting the 5' leader and immunoglobulin constant regions to
416 amplify multiple Ig isotypes, followed by nested PCR for specific amplification of HC and
417 LC variable regions and incorporation of homologous sequences compatible with expression
418 vectors. PCR products were analyzed on 1% agarose gels, and fragments of approximately
419 500 bp (HC) and 450 bp (LC) were purified, linearized, and used for small-scale antibody
420 expression.

421

422 **Single-cell BCR sequencing and antibody gene screening**

423 Antigen-specific memory B cells were sorted and loaded onto a Chromium Next GEM
424 Chip (10x Genomics). Single-cell capture, lysis, and first-strand cDNA synthesis were
425 performed using the Chromium Single Cell 5' Library & Gel Bead Kit (10x Genomics)
426 according to the manufacturer's instructions. Gene expression and V(D)J libraries were
427 generated using the Chromium Single Cell V(D)J Reagent Kits (10x Genomics). Libraries
428 were sequenced on an Illumina NovaSeq X Plus platform in paired-end 150-bp mode.

429 Single-cell BCR sequencing data were assembled and initially annotated using the V(D)J

430 module of Cell Ranger (v7.2), with the GRCh38 Human V(D)J reference dataset (GRCh38-
431 alts-ensembl-7.1.0) downloaded from 10x Genomics. Among a total of 1,959 cells, 1,894
432 cells contained productive V-J spanning pairs. Antibody clonal lineage identification was
433 performed using an optimized Change-O workflow. Human IG reference sequences from the
434 IMGT database were used for IgBLAST annotation and germline reconstruction, while Cell
435 Ranger V(D)J annotation results were additionally incorporated for single-cell BCR datasets.

436 To determine the clonal clustering threshold, nearest-neighbor distances between
437 productive BCR heavy-chain sequences were calculated using the `distToNearest` function in
438 the shazam package. Junction nucleotide sequences sharing identical V- and J-gene
439 assignments were compared using normalized Hamming distances. The resulting nearest-
440 neighbor distance distribution typically exhibits a bimodal pattern, representing intra-clonal
441 diversification driven by SHM and inter-clonal sequence diversity, respectively. A Gaussian
442 mixture model (GMM) was fitted to the nearest-neighbor distance distribution using the
443 `findThreshold` function with the `gmm` method. The threshold separating clonally related
444 and unrelated sequences was defined as the intersection between the two inferred Gaussian
445 components. This threshold (0.285103) was subsequently used for clone assignment in
446 downstream repertoire analyses.

447 Candidate antibodies for downstream characterization were selected from all identified
448 BCR repertoires according to the following criteria: (i) complete paired heavy- and light-
449 chain sequences detected within the same single cell; (ii) SHM rate greater than 3%; (iii)
450 heavy-chain CDRH3 length greater than 17 amino acids; and (iv) light-chain CDRL3 length
451 greater than 8 amino acids.

452

453 **Expression and purification of mAbs**

454 For antibodies derived from single B-cell PCR, purified PCR products were assembled
455 into linear human IgG expression cassettes by overlapping PCR as previously described². For
456 antibodies identified by single-cell BCR sequencing, heavy- and light-chain variable genes
457 were synthesized and cloned into mammalian expression vectors. Expression cassettes or
458 plasmids were transiently transfected into Expi293F cells using PEI MAX (Polysciences).
459 Culture supernatants containing recombinant IgGs were harvested for antibody quantification

460 and preliminary ELISA screening. For pseudovirus neutralization assays, antibody plasmids
461 were transfected into 15 mL Expi293F cultures, and antibodies were harvested after 5 days
462 and purified using protein A magnetic beads (GenScript, Cat # L00695).

463 For large-scale antibody production, heavy- and light-chain plasmids were co-transfected
464 into Expi293F cells at a 1:1.5 ratio using PEI MAX. Supernatants were collected 5 days post-
465 transfection, clarified by centrifugation, filtered through a 0.22- μ m membrane, and purified
466 by protein A affinity chromatography (SunResin, Cat # A4093101) on an ÄKTA system.
467 Bound antibodies were eluted with 100 mM glycine (pH 2.5), immediately neutralized with
468 1/10 volume of 1 M Tris-HCl, and buffer-exchanged into PBS.

469

470 **ELISA**

471 For preliminary screening, 96-well high-binding ELISA plates were coated overnight at
472 4 °C with glycoproteins (1 μ g/mL). Plates were washed three times with PBST (0.1% Tween-
473 20 in D-PBS) and blocked with 3% BSA in PBST for 2 h at 37 °C. Recombinant IgG-
474 containing supernatants (100 μ L/well) were added and incubated for 2 h at 37 °C. After five
475 washes, plates were incubated with HRP-conjugated anti-human IgG antibody (Promega, Cat
476 # W4031; 1:5,000 dilution) for 1 h at 37 °C. Plates were washed five times, developed with
477 TMB substrate (Beyotime, Cat # P0209) for 10 min at room temperature in the dark, and the
478 reaction was terminated with 50 μ L of 1 M sulfuric acid. Absorbance was measured at 450
479 nm.

480 For quantitative binding analysis, purified antibodies were serially diluted 3-fold from an
481 initial concentration of 10 μ g/mL and added to antigen-coated plates prepared as described
482 above. Incubation, washing, and detection procedures were performed under identical
483 conditions. All assays were performed in duplicate.

484

485 **Generation of pseudotyped VSVs**

486 All pseudotyped viruses were generated using pLVX plasmids encoding the M segment
487 of HTNV²⁹, SEOV³⁰, SNV²⁶, ANDV²⁷, LNV³¹, or JUQV³². HEK293T cells were seeded in
488 10-cm dishes and transfected 12 h later with M-segment expression plasmids (12 μ g),
489 psPAX2 (9 μ g), and pMD2.G (3 μ g) using PEI MAX. At 12 h post-transfection, the medium

490 was replaced with fresh culture medium. Lentivirus-containing supernatants were harvested
491 48 h later and stored at -80°C . Stable HEK293T cell lines expressing HTNV M, SEOV M,
492 SNV M, ANDV M, LNV M, or JUQV M were generated by lentiviral transduction followed
493 by puromycin selection.

494 For rVSV production, all pseudotyped viruses were produced according to previously
495 described protocols³³. Stable M-expressing HEK293T cells were seeded in 10-cm dishes and
496 infected 12 h later with rVSV-GFP or rVSV-luc for 1 h at 37°C . Cells were washed five times
497 with PBS and maintained in Opti-MEM containing 2% FBS. Supernatants containing rVSV-
498 HTNV, rVSV-SEOV, rVSV-SNV, rVSV-ANDV, rVSV-LNV, or rVSV-JUQV were collected
499 24-36 h post-infection, clarified by centrifugation, filtered through a $0.45\text{-}\mu\text{m}$ membrane, and
500 stored at -80°C until use.

501

502 **Pseudovirus neutralization assay**

503 Neutralization activity was evaluated using rVSV-based hantavirus pseudoviruses
504 expressing GFP, including rVSV-HTNV, rVSV-SEOV, rVSV-SNV, rVSV-ANDV, rVSV-LNV,
505 and rVSV-JUQV. Vero cells were seeded in 96-well plates at 5×10^3 cells per well one day
506 before infection. Antibodies were subjected to 3-fold serial dilution in complete medium and
507 pre-incubated with pseudoviruses for 1 h at 37°C . The antibody-virus mixtures were
508 subsequently transferred onto Vero cells and incubated for an additional 1 h at 37°C to
509 facilitate viral entry. Following incubation, cells were washed to remove unbound virus, and
510 fresh complete medium was added. Infection was assessed 24 h later by detection of GFP-
511 positive cells using fluorescence microscopy or an Operetta CLS high-content imaging
512 system (Perkin Elmer, HTECF-AW004). IC_{50} values were determined by fitting dose-response
513 curves with a four-parameter nonlinear regression model in GraphPad Prism 10.

514

515 **Authentic virus neutralization assay**

516 Neutralizing activity against authentic HTNV (strain 76118) was evaluated in Vero E6
517 cells using an immunofluorescence-based assay. Monoclonal antibodies were serially diluted
518 2-fold in complete culture medium and incubated with HTNV at the indicated dose (100
519 TCID_{50} per well) for 1 h at 37°C . The antibody and virus mixtures were subsequently

520 transferred to Vero cells seeded in 96-well plates and incubated at 37 °C for 1 h to facilitate
521 viral entry. After incubation, remove unbound viruses by washing, replenish with fresh
522 complete medium and incubate for another 72 hours. Following infection, culture
523 supernatants were removed, and cells were fixed and permeabilized with pre-chilled 80%
524 acetone for 30 min at room temperature. Plates were washed twice with PBST and incubated
525 with HTNV-NP-mAb³⁴ for 2 h at 37 °C. After washing, cells were stained with Alexa Fluor
526 488-conjugated goat anti-mouse IgG secondary antibody (Proteintech, Cat# SA00013-1;
527 1:400 dilution) for 1 h at 37 °C in the dark, followed by nuclear counterstaining with DAPI
528 (Proteintech, Cat# PR30021) for 15 min. Fluorescent signals were visualized using a
529 fluorescence microscope. Neutralization potency was quantified by calculating IC₅₀ values
530 using a four-parameter nonlinear regression model in GraphPad Prism 10.

531

532 **BLI**

533 Cross-competition and binding kinetics were characterized at 30 °C using an Octet R8
534 system (Sartorius). For epitope binning, HTNV Gn^HGc was immobilized onto HIS1K
535 biosensors (Sartorius) in assay buffer (D-PBS + 0.1% BSA). Following saturation with a
536 primary mAb, the sensors were exposed to a secondary mAb to monitor competitive binding.
537 Data were processed using the Epitope Binning module in Octet Analysis Studio, with signal
538 shifts recorded as relative light units (RLU).

539 For kinetic profiling, Gn^HGc -loaded sensors underwent a 120-s baseline equilibration
540 before immersion in serial three-fold dilutions of mAbs. Association and dissociation were
541 monitored for 300 s and 1,000 s, respectively. Sensors were regenerated with Glycine-HCl
542 (pH 1.7) between cycles. Binding kinetics were fitted using a 1:1 Langmuir binding model in
543 Octet Analysis Studio v13.0.2.46.

544

545 **Flow cytometry binding assay**

546 To evaluate antibody binding to different hantavirus glycoproteins, stable HEK293T cell
547 lines expressing individual M-segment proteins were generated, including HTNV²⁹, SEOV³⁰,
548 SNV²⁶, ANDV²⁷, LNV³¹, JUQV³², PUUV³⁵, DOBV³⁶, and CHOV (YP_009506070.1).
549 Briefly, 1 × 10⁶ cells were collected, washed, and resuspended in 100 μL PBS. Cells were

550 incubated with 10 μ g primary antibodies for 1 h on ice, followed by three washes with PBS to
551 remove unbound antibodies. Bound antibodies were detected using a PE anti-human IgG Fc
552 Antibody (Beyotime, Cat#410708) incubated for 1 h on ice in the dark. After three additional
553 washes, cells were resuspended in PBS and analyzed on a Cytex Aurora spectral flow
554 cytometer. Data were processed using FlowJo software, and antibody binding was quantified
555 as median fluorescence intensity (MFI).

556

557 ***In vivo* evaluation of mAb efficacy using rVSV pseudoviruses**

558 Luciferase-expressing pseudoviruses, including rVSV-HTNV, rVSV-SEOV, rVSV-SNV,
559 and rVSV-ANDV, were generated as described above. Female BALB/c mice (6 weeks old)
560 were inoculated intraperitoneally (i.p.) with the indicated pseudoviruses. At designated time
561 points post-inoculation, mice were anesthetized by intraperitoneal administration of 1%
562 pentobarbital sodium and subsequently injected i.p. with D-luciferin (1.5 mg per mouse;
563 Beyotime, Cat # ST198). Bioluminescence signals were acquired using a Lumina III in vivo
564 imaging system (Revvity), and three-dimensional optical tomographic reconstruction was
565 performed using the IVIS Spectrum imaging system (PerkinElmer).

566 For antibody pre-incubation assays, pseudoviruses were incubated with monoclonal
567 antibodies (6.25 mg/kg) at 37 °C for 1 h before i.p. administration into BALB/c mice.
568 Bioluminescence imaging was performed 6 h post-inoculation as described above. For
569 prophylactic protection experiments, monoclonal antibodies (6.25 mg/kg) were administered
570 i.p. 18 h before pseudovirus challenge, followed by in vivo imaging analysis 6 h after
571 infection. The pseudoviruses challenge works were conducted in an ABSL-2 facility, where
572 mice were provided with adequate food and water throughout the experiment. Ethical
573 approval for the animal challenge study was obtained from the Biosafety Committee of
574 Westlake University (Approval ID: AP # 25-164-LDP).

575

576 ***In vivo* evaluation of mAb efficacy using authentic virus**

577 The therapeutic efficacy of the antibody cocktail and IgG-scFv construct was evaluated
578 in neonatal BALB/c mice. Mice were challenged intraperitoneally with authentic HTNV
579 (strain 76118) at a dose of 5×10^5 PFU in 30 μ L per mouse. At 24 h post-infection, mice

580 received intraperitoneal administration of either the antibody cocktail (6.25 mg/kg), IgG-scFv
581 (6.25 mg/kg), or an isotype-matched human control antibody (6.25 mg/kg). Survival and body
582 weight were monitored for 25 days. To assess viral burden and tissue distribution, brain
583 samples were collected at the endpoint for quantitative PCR analysis. All the authentic HTNV
584 works were conducted in the ABSL-3 facility at Wuhan University, where mice were provided
585 with adequate food and water throughout the experiment. Ethical approval for the animal
586 challenge study was obtained from the Biosafety Committee of Wuhan University (Approval
587 ID: AP # WQ20210048).

588

589 **Immunofluorescence**

590 Tissues were fixed overnight at 4 °C in 4% paraformaldehyde, cryoprotected in 30%
591 sucrose for 48 h, and embedded in OCT compound. Cryosections (10 µm thickness) were
592 prepared for immunofluorescence analysis. Sections were fixed with 4% paraformaldehyde
593 for 10 min at room temperature, washed three times with PBS, and permeabilized with 0.25%
594 Triton X-100. After additional PBS washes, sections were blocked with 5% rat serum at room
595 temperature. Primary staining was performed for 1 h at room temperature using either anti-
596 GFP antibody (Abclonal, Cat # AE012; 1:100 dilution) or ascitic fluid from HTNV-Gn-
597 immunized mice (1:5,000 dilution). Following three washes with PBS, sections were
598 incubated with Alexa Fluor 488-conjugated goat anti-mouse IgG (H+L) secondary antibody
599 (Invitrogen, Cat # A-11029; 1:2000 dilution) for 1 h at room temperature. Sections were then
600 washed, mounted with DAPI-containing antifade mounting medium (Beyotime, Cat # P0131),
601 and imaged using a Zeiss LSM 900 inverted confocal microscope (Zeiss, WLL-W-20220039).

602

603 **Viral RNA extraction and quantification**

604 HTNV viral RNA was quantified by quantitative polymerase chain reaction (qPCR).
605 Total RNA was extracted from trizol homogenates (TaKaRa, Cat#9109) of brain tissues using
606 the high-throughput automatic nucleic acid extraction system (Thermo Fisher Scientific,
607 KingFisher Flex). Tissue weights were recorded before homogenization to enable
608 normalization. Viral RNA levels were quantified by two-step RT-qPCR. Reverse transcription
609 was performed using Hifair III SuperMix Plus (Yeasten, Cat# H7514240), followed by

610 quantitative PCR using Hieff qPCR SYBR Green Master Mix (Yeasen, Cat#WH2518011).
611 The HTNV NP segment was amplified using the following primers and probe: forward
612 primer, 5'-CAG TGC TAC CCT GCA AAG AA-3'; reverse primer, 5'-ATT GTT CGA TAC
613 GAT CAC TCC-3'; and probe, 5'-FAM/TCA TCC TCC TTG GAT ATG CAG GCC
614 TCA/BHQ1-3'. Reactions were carried out on an Archimed R4 Real-Time PCR Detection
615 System (ROCGENE) in a total volume of 20 μ L containing 1 μ L each of forward primer,
616 reverse primer, and probe, 5 μ L RT-PCR enzyme mix, 5 μ L RNA template, and 7 μ L
617 nuclease-free water. Thermal cycling conditions consisted of reverse transcription at 50 °C for
618 15 min, initial denaturation at 95 °C for 2 min, followed by 40 cycles of 95 °C for 5 s and
619 60 °C for 31 s, with fluorescence acquisition at each extension step. Relative viral RNA levels
620 were determined by comparative quantification using the mean Ct values of the HTNV NP
621 gene normalized to those of the housekeeping gene GAPDH. Relative expression levels were
622 calculated using the $2^{-\Delta\Delta C_t}$ method.

623

624 **Cryo-EM sample preparation and data collection**

625 For the hantavirus Gn^HGc-Fab complexes, purified Gn^HGc protein was mixed with XA-
626 044 or XA-3H12 at a molar ratio of 1:3 and incubated at 37°C for 1 h before loading onto a
627 Superose 200 Increase 10/300 column (GE Healthcare, 29091596) equilibrated in buffer
628 containing 50 mM Tris and 150 mM NaCl, pH 7.4. Fractions containing the complex were
629 concentrated using a 50-kDa molecular weight cut-off concentrator (Amicon Ultra
630 UFC510096). Protein quality was assessed by preparative size-exclusion chromatography
631 (Inscinstech Unique Autopre), SDS-PAGE and western blotting.

632 A 5 μ L aliquot of 0.1 mg/mL Gn^HGc-Fab complex was applied to freshly glow-
633 discharged holy carbon grids (Quantifoil R2/2, Cu 200 mesh; 30 s at 20 mA) and plunge-
634 frozen using a Vitrobot Mark IV (Thermo Fisher Scientific) with a blot force of 0, blot time
635 of 2 s, 80% humidity and 4°C. Data were collected using EPU software (Thermo Fisher
636 Scientific) to control an FEI Titan Krios G4 transmission electron microscope operated at 300
637 kV and equipped with a Falcon 4i Summit direct electron detector and a Selectris X energy
638 filter. Automated data collection was performed at a nominal magnification of 130,000 \times ,
639 corresponding to a pixel size of 0.97 Å. The dose rate was set to 7.78 counts per physical

640 pixel per second. In total, 14,202 movies of the SNV Gn^HGc-XA-044 complex and 16,555
641 movies of the HTNV Gn^HGc-XA-3H12 complex were collected, with defocus values ranging
642 from 0.9 to 1.8 μm .

643

644 **Cryo-EM model building and analysis**

645 UCSF ChimeraX and Coot were used to fit atomic models into the density maps,
646 including XA-044 heavy chain (PDB 7S0B), XA-044 light chain (PDB 7CZU), XA-3H12
647 heavy chain (PDB 7CZQ), XA-3H12 light chain (PDB 8R9Y), HTNV Gn (PDB 6Y6P),
648 HTNV Gc (PDB 5LJY), SNV Gn (PDB 8AHN) and SNV Gc (PDB 6Y5W)^{37,38}. The full
649 complex and Gn^HGc-Fab regions were then manually rebuilt in Coot³⁷. The models were
650 refined using Rosetta³⁹. Figures were generated using UCSF ChimeraX³⁸. Protein-protein
651 interactions have been analyzed by PISA⁴⁰.

652

653 **Quantification and Statistical Analysis**

654 GraphPad Prism 10 software was used for data visualization and statistical analyses.
655 Statistical comparisons between two groups were performed using unpaired, two-tailed
656 Mann-Whitney test. Data are presented as mean \pm SEM unless otherwise indicated. Statistical
657 significance was defined as ns (not significant, $p \geq 0.05$), * $p < 0.05$, ** $p < 0.01$, *** $p <$
658 0.001 , and **** $p < 0.0001$.

659

660 **ACKNOWLEDGMENTS**

661 We thank the technical support from the Biomedical Research Core Facility, Laboratory
662 Animal Resources Center, Cryo-EM Facility and High-Performance Computing Center at
663 Westlake University. We thank Chi Biotech Co., Ltd. for assisting in the single-cell
664 sequencing. This work was supported by Westlake Education Foundation (to D.L. and Z.W.),
665 Zhejiang Provincial Key Laboratory Construction Project (2024ZY01026), the National
666 Natural Science Foundation of China (82471858 to D.L. and 82272330 to X.W.), Zhejiang
667 Provincial Natural Science Foundation of China (LR26C080001 to D.L.), the National Key R
668 and D Program of China (2023YFC2605504 to W.H. and 2024YFA1306600 to Z.W.), the
669 Science and Technology Program of Science, Technology and Innovation Commission of

670 Shenzhen Municipality (JCYJ20230807090209018 to W.H.), the Shaanxi Provincial Natural
671 Science Basic Research Program Key Project (2024JC-ZDXM-42 to R.L. and 2025JC-
672 YBMS-988 to Z.L.), and the Assistance Program of Xijing Hospital (XJZT26JS05 to R.L.).

673

674 **DATA AVAILABILITY**

675 The data and codes that support the findings of this study are available from the
676 corresponding authors on request.

677

678 **AUTHOR CONTRIBUTIONS**

679 J.Y., Z.J., Y.K., and Z.L. performed experiments. Z.D. performed computational analysis.
680 X.Z., X.D., and J.L. collected human specimens and provided clinical support. Y.K. and Z.W.
681 performed structural studies and analysis. Z.L., X.W., and R.L. conducted and supervised
682 authentic virus *in vitro* studies. Z.J., S.C., L.N., F.L., and W.H. performed and supervised the
683 authentic virus *in vivo* study. J.B., M.L., J.S., Z.Z., F.Y., R.S. and Z.K. provided critical
684 scientific guidance. D.L. conceived, designed, and supervised the study. J.Y., Z.W. and D.L.
685 wrote the paper. All authors reviewed and approved the manuscript.

686

687 **DECLARATION OF INTERESTS**

688 D.L., J.Y., R.L., Z.L., X.Z., X.W., J.L., X.D. have applied for patents concerning HTNV
689 antibodies that are related to this work. All other authors declare no conflict of interest.

690

691 **REFERENCES**

- 692 1 Kuhn, J. H. & Schmaljohn, C. S. A Brief History of Bunyaviral Family Hantaviridae.
693 *Diseases* **11**, doi:10.3390/diseases11010038 (2023).
- 694 2 Kruger, D. H., Figueiredo, L. T., Song, J. W. & Klempa, B. Hantaviruses--globally
695 emerging pathogens. *J Clin Virol* **64**, 128-136, doi:10.1016/j.jcv.2014.08.033 (2015).
- 696 3 Engdahl, T. B. *et al.* Broad and potently neutralizing monoclonal antibodies isolated
697 from human survivors of New World hantavirus infection. *Cell Rep* **35**, 109086,
698 doi:10.1016/j.celrep.2021.109086 (2021).
- 699 4 Jonsson, C. B., Figueiredo, L. T. & Vapalahti, O. A global perspective on hantavirus

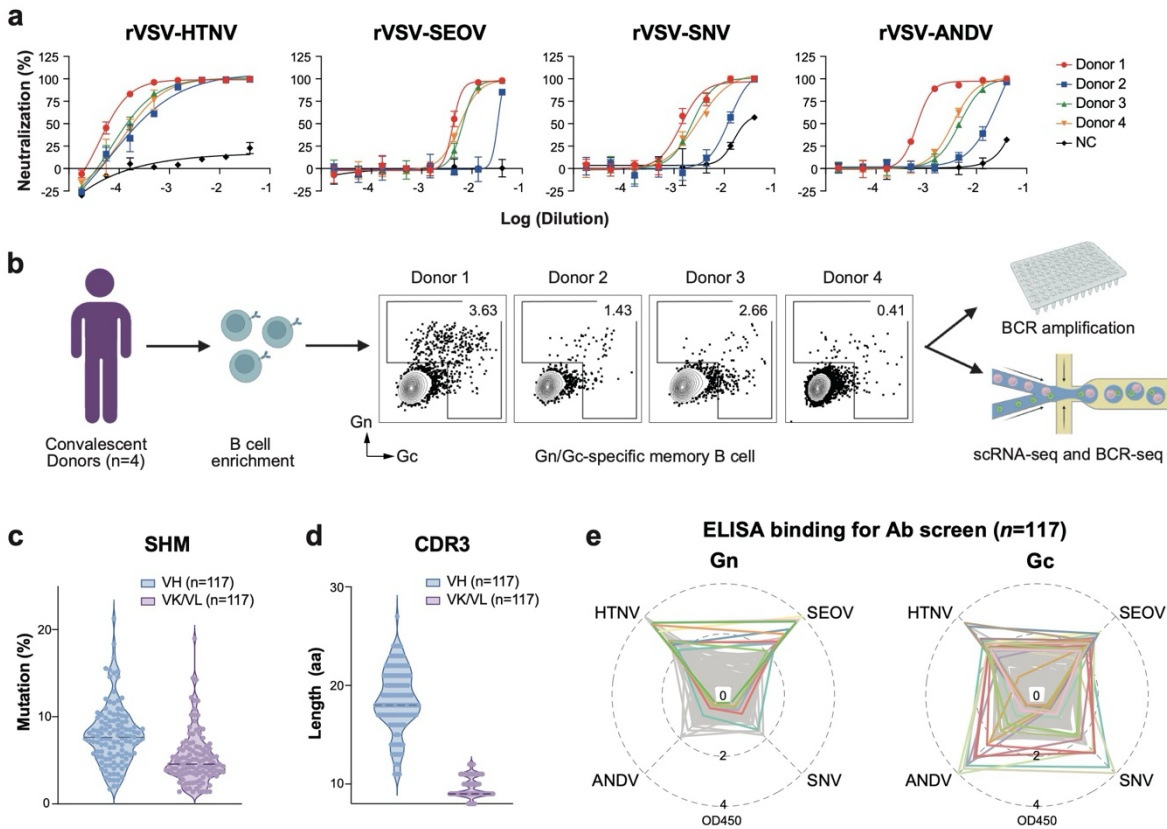
- 700 ecology, epidemiology, and disease. *Clin Microbiol Rev* **23**, 412-441,
701 doi:10.1128/CMR.00062-09 (2010).
- 702 5 Vapalahti, O. *et al.* Hantavirus infections in Europe. *Lancet Infect Dis* **3**, 653-661,
703 doi:10.1016/s1473-3099(03)00774-6 (2003).
- 704 6 Vial, P. A. *et al.* Hantavirus in humans: a review of clinical aspects and management.
705 *Lancet Infect Dis* **23**, e371-e382, doi:10.1016/S1473-3099(23)00128-7 (2023).
- 706 7 Figueiredo, L. T., Souza, W. M., Ferres, M. & Enria, D. A. Hantaviruses and
707 cardiopulmonary syndrome in South America. *Virus Res* **187**, 43-54,
708 doi:10.1016/j.virusres.2014.01.015 (2014).
- 709 8 Watson, D. C. *et al.* Epidemiology of Hantavirus infections in humans: a
710 comprehensive, global overview. *Crit Rev Microbiol* **40**, 261-272,
711 doi:10.3109/1040841X.2013.783555 (2014).
- 712 9 Avsic-Zupanc, T., Saksida, A. & Korva, M. Hantavirus infections. *Clin Microbiol Infect*
713 **21S**, e6-e16, doi:10.1111/1469-0691.12291 (2019).
- 714 10 Afzal, S. *et al.* Hantavirus: an overview and advancements in therapeutic approaches
715 for infection. *Front Microbiol* **14**, 1233433, doi:10.3389/fmicb.2023.1233433 (2023).
- 716 11 Plyusnin, A., Vapalahti, O. & Vaheri, A. Hantaviruses: genome structure, expression
717 and evolution *The Journal of general virology* **77 (Pt 11)** (1996).
- 718 12 Serris, A. *et al.* The Hantavirus Surface Glycoprotein Lattice and Its Fusion Control
719 Mechanism. *Cell* **183**, 442-456 e416, doi:10.1016/j.cell.2020.08.023 (2020).
- 720 13 Guo, L. *et al.* High-resolution in situ structures of hantavirus glycoprotein tetramers.
721 *Cell* **189**, 2731-2747 e2715, doi:10.1016/j.cell.2026.01.030 (2026).
- 722 14 Rissanen, I. *et al.* Structural Transitions of the Conserved and Metastable Hantaviral
723 Glycoprotein Envelope. *J Virol* **91**, doi:10.1128/JVI.00378-17 (2017).
- 724 15 Guardado-Calvo, P. *et al.* Mechanistic Insight into Bunyavirus-Induced Membrane
725 Fusion from Structure-Function Analyses of the Hantavirus Envelope Glycoprotein Gc.
726 *PLoS Pathog* **12**, e1005813, doi:10.1371/journal.ppat.1005813 (2016).
- 727 16 Willensky, S. *et al.* Crystal Structure of Glycoprotein C from a Hantavirus in the Post-
728 fusion Conformation. *PLoS Pathog* **12**, e1005948, doi:10.1371/journal.ppat.1005948
729 (2016).

- 730 17 Heiskanen, T. *et al.* Phage-displayed peptides mimicking the discontinuous
731 neutralization sites of puumala Hantavirus envelope glycoproteins. *Virology* **262**, 321-
732 332, doi:10.1006/viro.1999.9930 (1999).
- 733 18 Stass, R. *et al.* Mechanistic basis for potent neutralization of Sin Nombre hantavirus by
734 a human monoclonal antibody. *Nat Microbiol* **8**, 1293-1303, doi:10.1038/s41564-023-
735 01413-y (2023).
- 736 19 Levanov, L., Iheozor-Ejiofor, R. P., Lundkvist, A., Vapalahti, O. & Plyusnin, A.
737 Defining of MAbs-neutralizing sites on the surface glycoproteins Gn and Gc of a
738 hantavirus using vesicular stomatitis virus pseudotypes and site-directed mutagenesis.
739 *J Gen Virol* **100**, 145-155, doi:10.1099/jgv.0.001202 (2019).
- 740 20 Mittler, E. *et al.* Human antibody recognizing a quaternary epitope in the Puumala virus
741 glycoprotein provides broad protection against orthohantaviruses. *Sci Transl Med* **14**,
742 eabl5399, doi:10.1126/scitranslmed.abl5399 (2022).
- 743 21 Mittler, E. *et al.* Structural and mechanistic basis of neutralization by a pan-hantavirus
744 protective antibody. *Sci Transl Med* **15**, eadg1855, doi:10.1126/scitranslmed.adg1855
745 (2023).
- 746 22 Higa, M. M., Petersen, J., Hooper, J. & Doms, R. W. Efficient production of Hantaan
747 and Puumala pseudovirions for viral tropism and neutralization studies. *Virology* **423**,
748 134-142, doi:10.1016/j.virol.2011.08.012 (2012).
- 749 23 Ray, N., Whidby, J., Stewart, S., Hooper, J. W. & Bertolotti-Ciarlet, A. Study of Andes
750 virus entry and neutralization using a pseudovirion system. *J Virol Methods* **163**, 416-
751 423, doi:10.1016/j.jviromet.2009.11.004 (2010).
- 752 24 Basu, M. & Fieldhouse, R. Hantavirus outbreak exposes uncertainty about how disease
753 spreads. *Nature*, doi:10.1038/d41586-026-01512-w (2026).
- 754 25 Liu, R. R. *et al.* Investigation of a subunit protein vaccine for HFRS based on a
755 consensus sequence between envelope glycoproteins of HTNV and SEOV. *Virus*
756 *Research* **334**, doi:10.1016/j.virusres.2023.199149 (2023).
- 757 26 Arikawa, J., Lapenotiere, H. F., Iacono-Connors, L., Wang, M. L. & Schmaljohn, C. S.
758 Coding properties of the S and the M genome segments of Sapporo rat virus:
759 comparison to other causative agents of hemorrhagic fever with renal syndrome.

- 760 *Virology* **176**, 114-125, doi:10.1016/0042-6822(90)90236-k (1990).
- 761 27 Meissner, J. D., Rowe, J. E., Borucki, M. K. & St Jeor, S. C. Complete nucleotide
762 sequence of a Chilean hantavirus. *Virus Res* **89**, 131-143, doi:10.1016/s0168-
763 1702(02)00129-6 (2002).
- 764 28 Li, D. *et al.* In vitro and in vivo functions of SARS-CoV-2 infection-enhancing and
765 neutralizing antibodies. *Cell* **184**, 4203-+, doi:10.1016/j.cell.2021.06.021 (2021).
- 766 29 Schmaljohn, C. S., Schmaljohn, A. L. & Dalrymple, J. M. Hantaan virus M RNA:
767 coding strategy, nucleotide sequence, and gene order. *Virology* **157**, 31-39,
768 doi:10.1016/0042-6822(87)90310-2 (1987).
- 769 30 Spiropoulou, C. F. *et al.* Genome structure and variability of a virus causing hantavirus
770 pulmonary syndrome. *Virology* **200**, 715-723, doi:10.1006/viro.1994.1235 (1994).
- 771 31 Johnson, A. M. *et al.* Laguna Negra virus associated with HPS in western Paraguay and
772 Bolivia. *Virology* **238**, 115-127, doi:10.1006/viro.1997.8840 (1997).
- 773 32 Spruill-Harrell, B. *et al.* Purifying selection constrains the evolution of Jujuitiba virus
774 in wild *Oligoryzomys nigripes* communities. *PLoS Pathog* **22**, e1013839,
775 doi:10.1371/journal.ppat.1013839 (2026).
- 776 33 Whitt, M. A. Generation of VSV pseudotypes using recombinant DeltaG-VSV for
777 studies on virus entry, identification of entry inhibitors, and immune responses to
778 vaccines. *J Virol Methods* **169**, 365-374, doi:10.1016/j.jviromet.2010.08.006 (2010).
- 779 34 Liu, R. *et al.* HTNV infection of CD8(+) T cells is associated with disease progression
780 in HFRS patients. *Commun Biol* **4**, 652, doi:10.1038/s42003-021-02182-2 (2021).
- 781 35 Vapalahti, O., Kallio-Kokko, H., Salonen, E. M., Brummer-Korvenkontio, M. & Vaheri,
782 A. Cloning and sequencing of Puumala virus Sotkamo strain S and M RNA segments:
783 evidence for strain variation in hantaviruses and expression of the nucleocapsid protein.
784 *J Gen Virol* **73 (Pt 4)**, 829-838, doi:10.1099/0022-1317-73-4-829 (1992).
- 785 36 Nemirov, K. *et al.* Genetic characterization of new Dobrava hantavirus isolate from
786 Greece. *J Med Virol* **69**, 408-416, doi:10.1002/jmv.10304 (2003).
- 787 37 Emsley, P., Lohkamp, B., Scott, W. G. & Cowtan, K. Features and development of Coot.
788 *Acta Crystallogr D Biol Crystallogr* **66**, 486-501, doi:10.1107/S0907444910007493
789 (2010).

- 790 38 Pettersen, E. F. *et al.* UCSF ChimeraX: Structure visualization for researchers,
791 educators, and developers. *Protein Sci* **30**, 70-82, doi:10.1002/pro.3943 (2021).
- 792 39 Wang, R. Y. *et al.* Automated structure refinement of macromolecular assemblies from
793 cryo-EM maps using Rosetta. *Elife* **5**, doi:10.7554/eLife.17219 (2016).
- 794 40 Krissinel, E. & Henrick, K. Inference of macromolecular assemblies from crystalline
795 state. *J Mol Biol* **372**, 774-797, doi:10.1016/j.jmb.2007.05.022 (2007).
- 796
- 797

1 **FIGURES AND FIGURE LEGENDS**



2

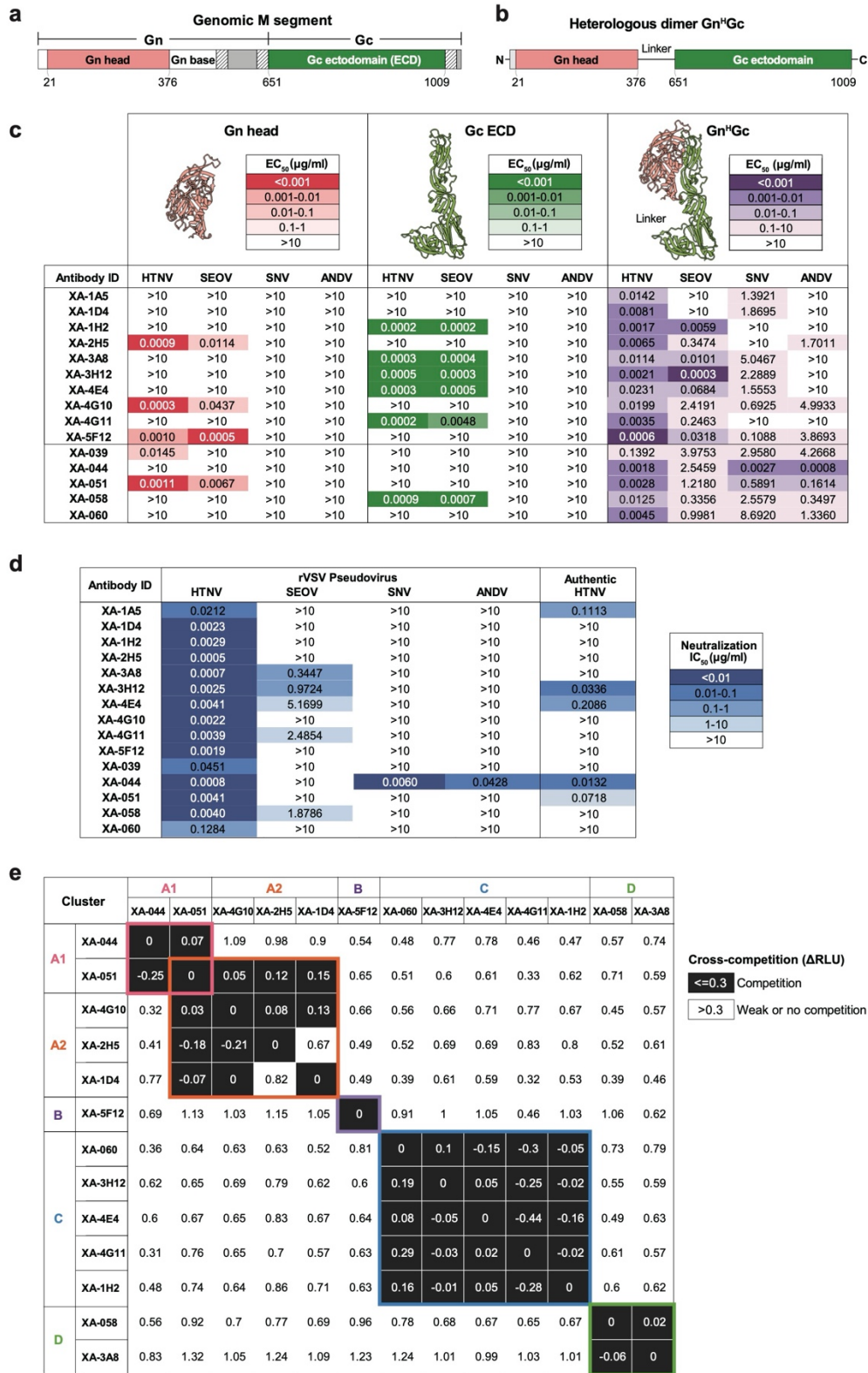
3 **Fig. 1 | Isolation of cross-reactive antibodies from HFRS convalescent patients.**

4 **a**, Plasma neutralization of GFP-encoding pseudotyped rVSV bearing HTNV, SEOV, SNV, or ANDV
 5 glycoproteins. Plasma samples were collected from four convalescent HFRS donors and a healthy donor
 6 as the negative control (NC). Percent neutralization was plotted against \log_{10} -transformed plasma dilution,
 7 and relative infectivity was quantified by GFP-positive cells. Data represent mean \pm SEM from two inde-
 8 dependent replicates.

9 **b**, Workflow for antigen-specific memory B cell isolation. B cells were enriched by negative selection,
 10 and HTNV- or SEOV-Gn/Gc-specific IgM⁻IgD⁻ B cells were sorted by FACS for single-cell PCR and
 11 BCR sequencing.

12 **c,d**, Somatic hypermutation (SHM) frequencies (**c**) and CDR3 length distributions (**d**) in V_H and V_K/V_L
 13 genes of Gn/Gc-specific BCRs obtained by single-cell PCR (n=49) or single-cell BCR sequencing
 14 (n=68).

15 **e**, ELISA-based screening of antibody binding breadth. Radar plots show antibody reactivity to Gn (left
 16 panel) and Gc (right panel) of HTNV, SEOV, SNV, and ANDV, with concentric rings indicating OD₄₅₀
 17 values.



18

19 Fig. 2 | Identification of NABs targeting distinct hantavirus Gn/Gc neutralization sites.

20 **a**, Scheme of the hantavirus M segment domain organization, with individual protein domains indicate
21 color-coded.

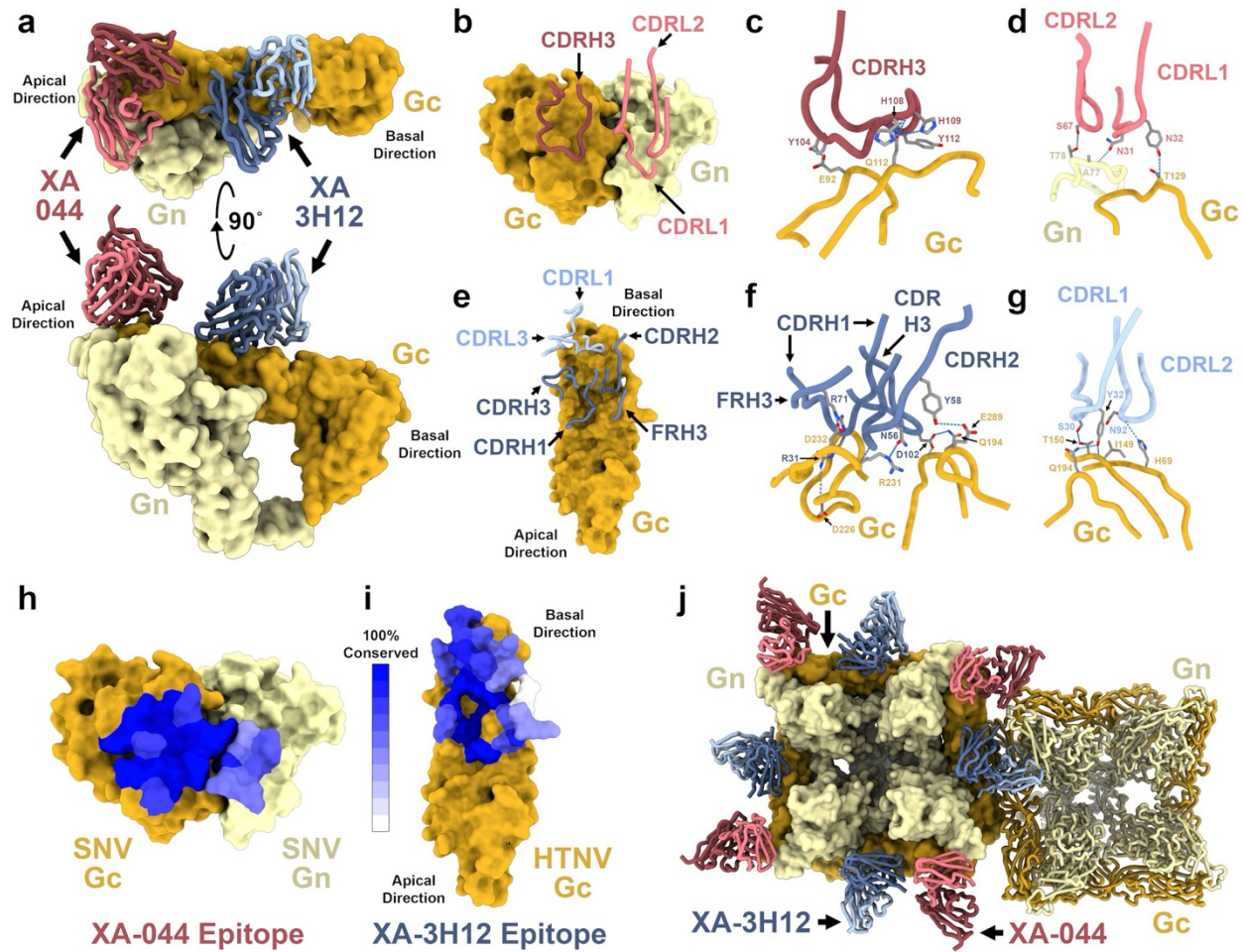
22 **b**, Scheme of the single-chain hantavirus glycoprotein heterodimer Gn^HGc construct.

23 **c**, Binding profiles of the downselected neutralizing antibodies. Recombinant Gn head, Gc ectodomain
24 (ECD), and Gn^HGc proteins from HTNV, SEOV, SNV, and ANDV were analyzed by ELISA. Color inten-
25 sity denotes binding EC₅₀. Data represent mean ± SEM from two independent experiments.

26 **d**, Neutralization potency against pseudotyped rVSVs of HTNV, SEOV, SNV, and ANDV, as well as au-
27 thentic HTNV. Color intensity denotes IC₅₀ neutralization titers. Data represent mean ± SEM from two
28 independent experiments.

29 **e**, Epitope binning by BLI-based competition analysis. HTNV Gn^HGc antigen was captured by a primary
30 antibody (y axis), followed by binding of a secondary antibody (x axis). Secondary-antibody responses
31 were normalized to maximal uncompleted binding. Antibody pairs were classified as competing (black,
32 ≤0.3) or weakly/non-competing (white, >0.3), and grouped by cross-competition profiles.

33



34

35 **Fig. 3 | Cryo-EM structure of the two distinct neutralization epitopes.**

36 **a**, XA-044 and XA-3H12 superposed onto the ANDV Gn-Gc dimer (PDB: 9P3Y), showing epitope loca-
 37 tions. Fabs are shown as ribbons and Gn-Gc as surface; Gn, yellow; Gc, gold; XA-044 heavy/light chains,
 38 dark/light red; XA-3H12 heavy/light chains, dark/light blue.

39 **b**, Focused view of XA-044 CDRH/CDRL binding at the SNV Gn-Gc apical interface.

40 **c,d**, Zoomed-in views of the SNV Gn-Gc interface with the XA-044 heavy (**c**) or light (**d**) chain, with se-
 41 lected side chains shown as sticks. Hydrogen bonds and salt bridges are shown as cyan dashed lines.

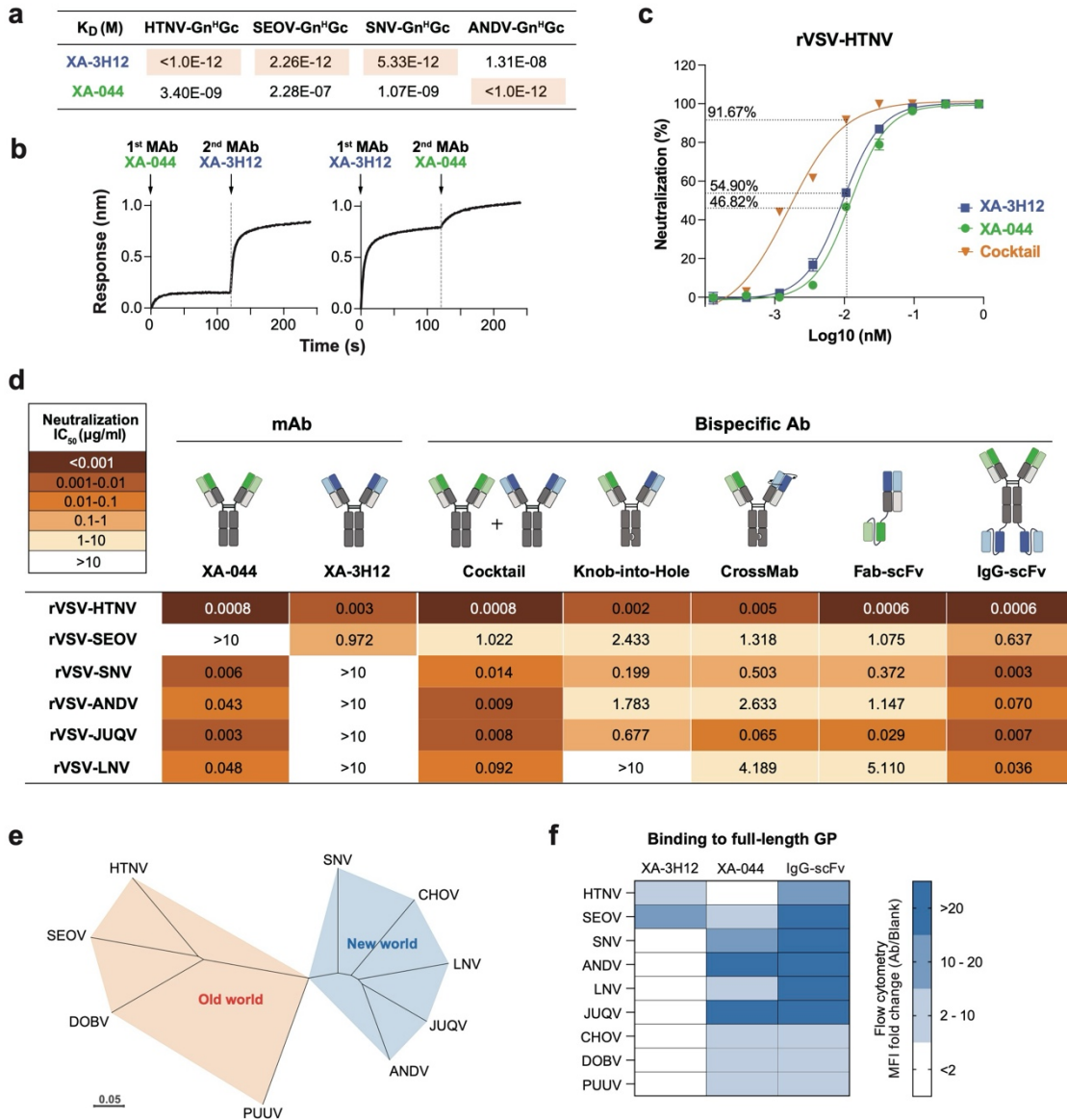
42 **e**, Focused view of XA-3H12 CDRH/CDRL binding to the basal region of HTNV Gc domain II.

43 **f,g**, Zoomed-in views of the HTNV Gc interface with the XA-3H12 heavy (**f**) or light (**g**) chain, annotated
 44 as in (**c**) and (**d**).

45 **h,i**, Molecular surface of XA-044 (**h**) and XA-3H12 (**i**) epitopes on SNV Gn-Gc and HTNV Gc, respec-
 46 tively, colored by hantavirus residue conservation using a 10-step Clustal Omega gradient from deep blue
 47 to white, corresponding to scores of 100 to 0.

48 **j**, XA-044 and XA-3H12 super-positioned onto ANDV Gn-Gc tetramer with neighboring tetramer (PDB

49 ID: 9P3Y and 9P3X), where main tetramer rendered in surface and neighboring tetramer in ribbon. Color
50 scheme is the same as in (a).
51



52

53 **Fig. 4 | Bispecific antibody strategies achieve pan-hantavirus neutralization.**

54 **a.** Binding affinities of XA-3H12 and XA-044. Binding kinetics to HTNV-, SEOV-, SNV-, and ANDV-
55 Gn^HGc were measured by BLI and fit to a 1:1 Langmuir model. Affinities are reported as K_D values.

56 **b.** Competition analysis between XA-044 and XA-3H12 by BLI. Recombinant HTNV Gn^HGc was satu-
57 rated with the first antibody, followed by incubation with the second neutralizing antibody to assess com-
58 petitive binding.

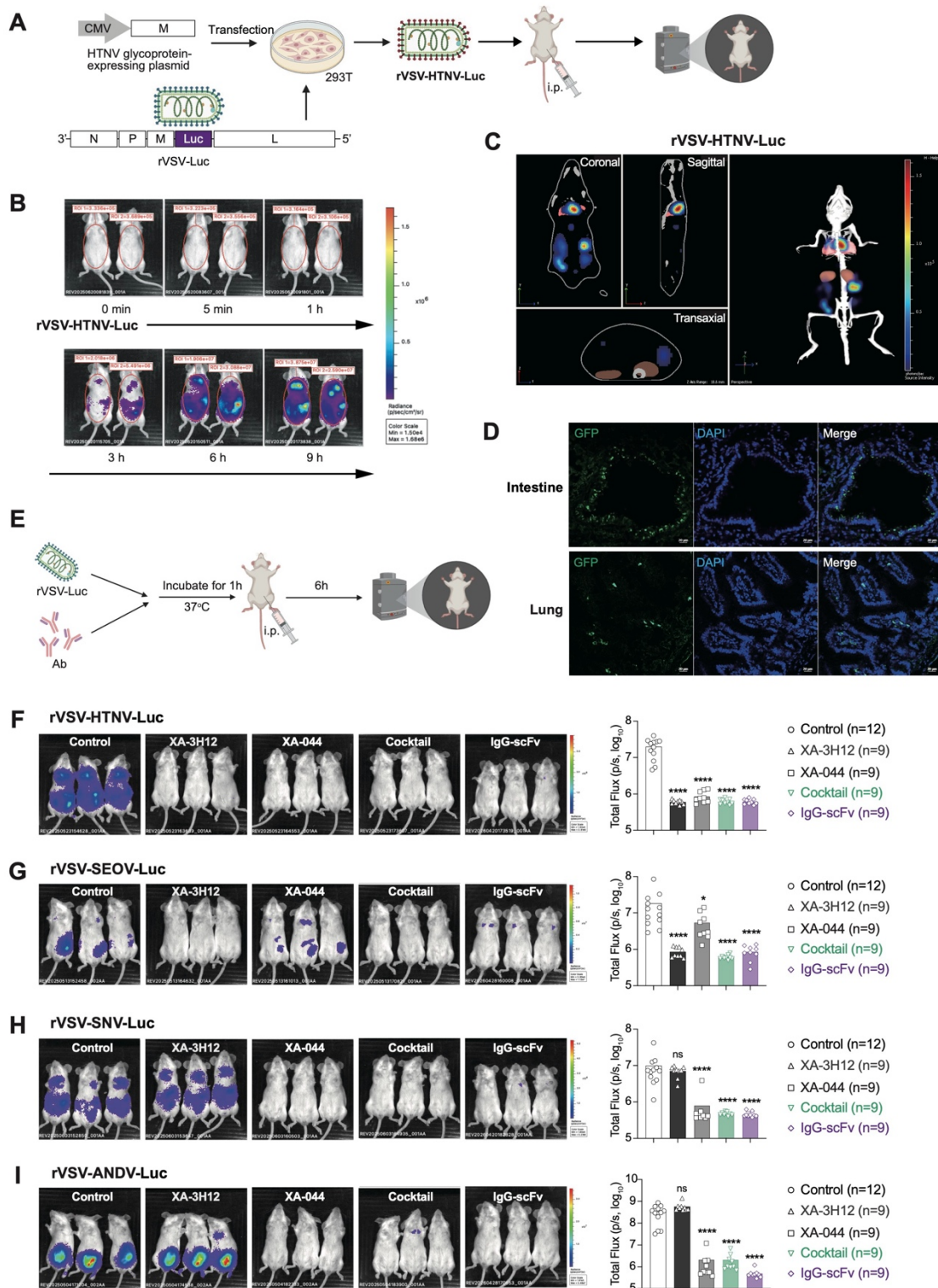
59 **c.** Synergistic neutralization by XA-044 and XA-3H12. Based on experimentally determined IC₅₀ values,
60 XA-044 (0.0051 nM) and XA-3H12 (0.0160 nM) were mixed at a 1:1 volume ratio, using their respective
61 IC₅₀ concentrations as the reference concentration (0.0106 nM). The mixture was then subjected to 3-fold
62 serial dilutions above and below 1× and tested in standard neutralization assays. Neutralization (%) at the

63 combined IC₅₀ concentration is indicated by dashed lines and annotated. Data represent mean ± SEM
64 from two independent experiments.

65 **d.** Neutralization breadth and potency of parental antibodies, antibody cocktail, and bispecific antibodies.
66 Neutralizing activities were evaluated against six hantavirus pseudoviruses. Color intensity denotes neu-
67 tralization IC₅₀ values across viral strains and antibody formats. Data represent mean ± SEM from two
68 independent experiments.

69 **e,f.** Flow cytometric analysis of antibody binding to cell-surface-expressed full-length hantavirus glyco-
70 protein (GP). **(e)** Phylogenetic analysis of representative Old World and New World hantaviruses included
71 in the flow cytometry assay. **(f)** Heatmap summarizing antibody-binding activity, quantified by mean flu-
72 orescence intensity (MFI) from flow cytometry.

73



74

75 **Fig. 5 | A pseudovirus reporter system enables *in vivo* evaluation of hantavirus entry blockade.**

76 **a**, Schematic of the pseudovirus *in vivo* infection model. Hantavirus glycoproteins were expressed on

77 HEK293T cells, which were then infected with luciferase-expressing rVSV-Luc to generate rVSV-

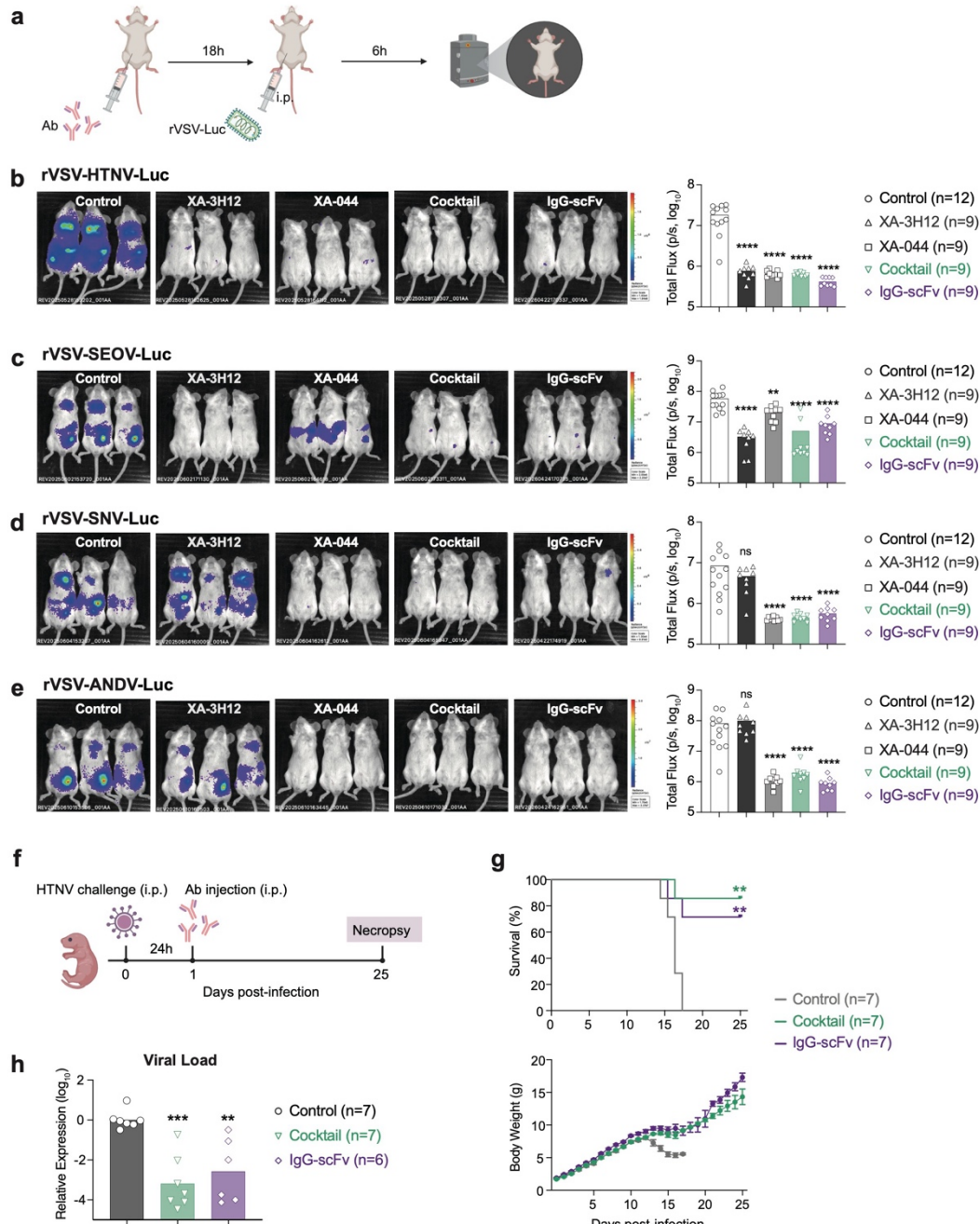
78 HTNV-Luc pseudoviruses. Pseudoviruses were administered to mice by intraperitoneal (i.p.) injection,
79 and infection was quantified by *in vivo* bioluminescence imaging.

80 **b**, Temporal dynamics of bioluminescence in rVSV-HTNV-inoculated mice. Live-animal imaging was
81 performed at the indicated time points, with all images displayed on the same scale.

82 **c**, Representative three-dimensional bioluminescence imaging of rVSV-HTNV-inoculated mice at 6 h
83 post-inoculation using the IVIS Spectrum system.

84 **d**, Immunofluorescence analysis of rVSV-HTNV infection in the intestine (upper panels) and lung (lower
85 panels) collected 6 h after inoculation. GFP-expressing rVSV-Luc pseudoviruses were used. GFP-positive
86 signals are shown in green, and nuclei were counterstained with DAPI (blue). Scale bars, 75 μm .

87 **e-i** Antibody-mediated blockade of pseudovirus entry in mice. **(e)** Experimental design. Luciferase-ex-
88 pressing **(f)** rVSV-HTNV-Luc, **(g)** rVSV-SEOV-Luc, **(h)** rVSV-SNV-Luc, or **(i)** rVSV-ANDV-Luc pseu-
89 doviruses were preincubated with neutralizing antibodies before i.p. administration into BALB/c mice.
90 Bioluminescence was measured at 6 h post-inoculation. Representative images are shown on the left, with
91 quantified bioluminescence intensities on the right. Statistical significance was determined using the
92 Mann-Whitney test. ns, not significant; $p \geq 0.05$; * $p < 0.05$; ** $p < 0.01$; *** $p < 0.001$; **** $p < 0.0001$.
93

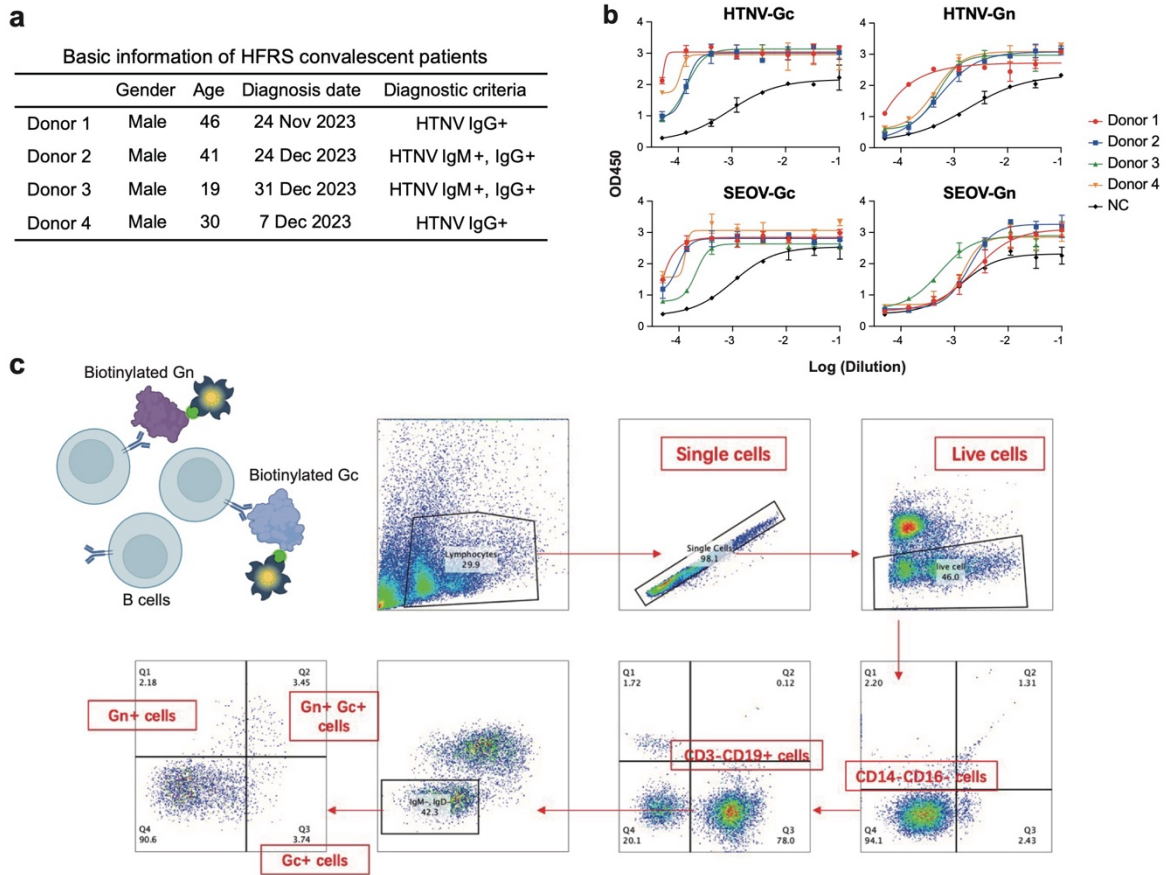


94

95 **Fig. 6 | Bispecific strategies confer broad protection *in vivo*.**

96 **a-e**, Prophylactic treatment prevented pseudovirus entry in mice. **(a)** Experimental design. Antibodies
 97 were i.p. administered into BALB/c mice 18 h prior to challenge with luciferase-expressing **(b)** rVSV-
 98 HTNV-Luc, **(c)** rVSV-SEOV-Luc, **(d)** rVSV-SNV-Luc, or **(e)** rVSV-ANDV-Luc pseudoviruses. Bio-lumi-
 99 nescence was measured at 6 h post-inoculation. Representative images are shown on the left, with quanti-
 100 fied bioluminescence intensities on the right.

101 **f-i**, Post-exposure therapy protected neonatal mice from lethal HTNV challenge. **(f)** Experimental design.
102 Neonatal BALB/c mice were challenged i.p. with authentic HTNV and received i.p. administration of the
103 antibody cocktail, IgG-scFv, or isotype control antibody at 24 h post-infection. **(g)** Survival curves and
104 body weight changes. **(h)** Viral RNA loads in brain. Statistical significance was determined using the
105 Mann-Whitney test. ns, not significant; $p \geq 0.05$; * $p < 0.05$; ** $p < 0.01$; *** $p < 0.001$; **** $p < 0.0001$.
106



108

109 **Extended Data Fig. 1 | Antigen-specific B cell sorting from HFRS convalescent donors.**

110 **a**, Clinical characteristics of four HFRS convalescent donors diagnosed in 2023. Donors were confirmed
 111 to be HTNV IgG-positive and/or IgM-positive during hospitalization. Peripheral blood was collected dur-
 112 ing convalescence, approximately 6 months after discharge, after informed consent.

113 **b**, Plasma binding to HTNV and SEOV Gn and Gc from four convalescent HFRS donors was measured
 114 by ELISA. Plasma from a healthy donor was used as the negative control (NC). Data represent mean ±
 115 SEM from two independent experiments.

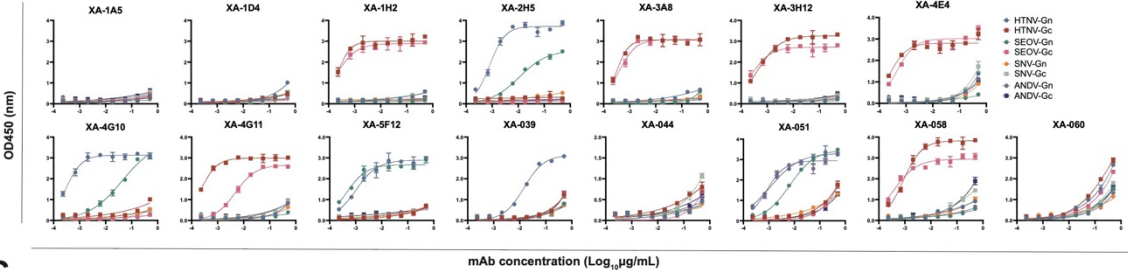
116 **c**, Representative flow-cytometric gating strategy for single-cell sorting of antigen-specific memory B
 117 cells recognizing HTNV-Gn, HTNV-Gc, SEOV-Gn, or SEOV-Gc.

118

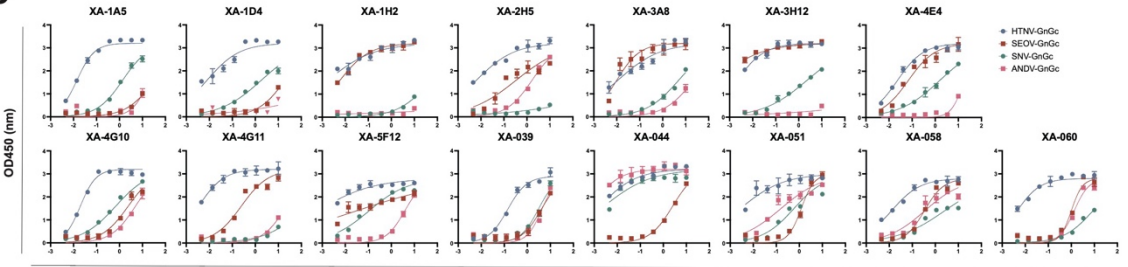
A

Group	MAb	Donor	Heavy chain variable gene sequence				Light chain variable gene sequence						
			CDR3 length (aa)	Mutation rate (%)	V-gene and allele	J-gene and allele	CDR3 length (aa)	Mutation rate (%)	V-gene and allele	J-gene and allele			
Single cell PCR	1H2	Donor 1											
	1D4	Donor 1	AKDGPIMFGLVEV	13	95.59	IGHV3-30*18	IGHJ8*02	QAWDRSTVI	9	93.80	IGLV3-1*01	IGLJ2*01	
	4G10	Donor 4	ARSCYCGGCGYYMYMDV	17	94.85	IGHV1-69*09	IGHJ8*03	GTWETIGRAWV	11	94.22	IGLV1-51*01	IGLJ3*02	
	3A8	Donor 3	VRDSYCSGGSCYSTNWFDL	20	94.24	IGHV3-33*01	IGHJ5*02	TSYTSRSTVL	10	95.92	IGLV2-14*03	IGLJ2*01	
	2H5	Donor 2	ARDQTGGWASGF	11	95.61	IGHV3-21*01	IGHJ4*02	VTWDDSLNGIL	11	95.56	IGLV1-44*01	IGLJ2*01	
	1A5	Donor 1	ARSSGWFGGAFDI	14	93.17	IGHV1-3*01	IGHJ3*02	SSYVGTNNVI	10	96.26	IGLV2-8*01	IGLJ2*01	
	3H12	Donor 3	ASTPGYDTPWYGPVR	15	93.22	IGHV3-44D*06	IGHJ4*02	QKYNMAPFT	9	97.89	IGKV1-2*01	IGKJ3*01	
	4E4	Donor 4	SAKDSQYSSQVRDVFVDV	18	90.97	IGHV3-53*04	IGHJ3*01	QKYNAPWIT	9	97.89	IGKV1-2*01	IGKJ1*01	
	4G11	Donor 4	VCDYMWGTFIDY	12	89.09	IGHV3-53*04	IGHJ4*02	QNYDHWPKT	9	93.71	IGKV1-2*01	IGKJ1*01	
	5F12	Donor 4	ARATFNQYVWQYKRDYLDY	21	98.30	IGHV3-33*01	IGHJ4*02	QQYNSYSRT	9	95.80	IGKV1-5*04	IGKJ1*01	
Single cell BCR-seq	HT-SNY-38	/	AREAVASRTYNNWFDP	17	85.03	IGHV4-59*01	IGHJ5*02	QSYDSSLGSGV	11	95.65	IGLV1-40*01	IGLJ3*02	
	HT-SNY-44	/	ATGVRYGELHPQYFYGMVDV	21	91.78	IGHV3-23*01, IGHV3-23*02, IGHV3-23D*01	IGHJ8*02	QQSFSPWIT	9	94.70	IGKV1-39*01, IGLK1D-39*01	IGKJ1*01	
	HT-SNY-51	/	TGYSGASCYSPYLYLDN	18	91.22	IGHV3-30*18, IGHV3-30*5*01	IGHJ4*02	QQSYSPWIT	9	94.72	IGKV1-39*01, IGLK1D-39*01	IGKJ1*01	
	HT-SNY-58	/	ARDRGGQRNDNWSRFYMDV	19	91.64	IGHV4-61*02	IGHJ8*03	QQSFGTPTT	9	95.78	IGKV1-39*01, IGLK1D-39*01	IGKJ2*01	
	HT-SNY-60	/	VRFGCSRSTQCRPNYFDP	19	91.53	IGHV3-30*03, IGHV3-30*04, IGHV3-30*19	IGHJ5*02	GSYTGSTWV	10	95.92	IGLV2-14*03	IGLJ3*02	

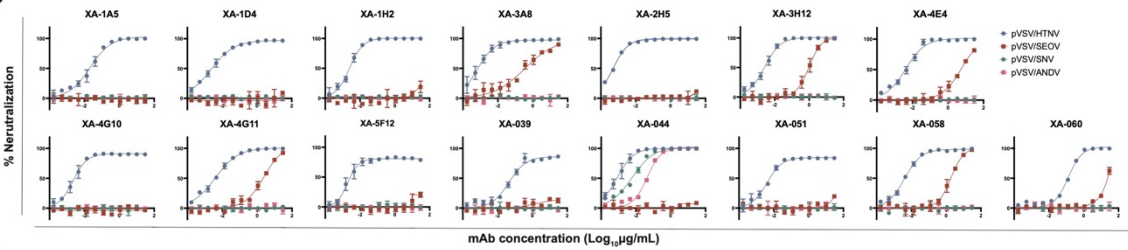
B



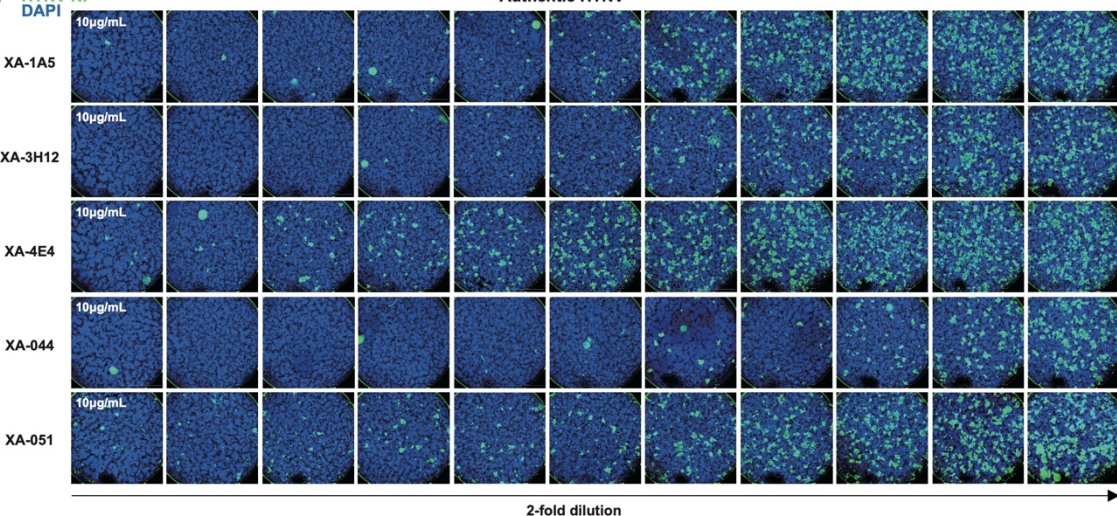
C



D



E



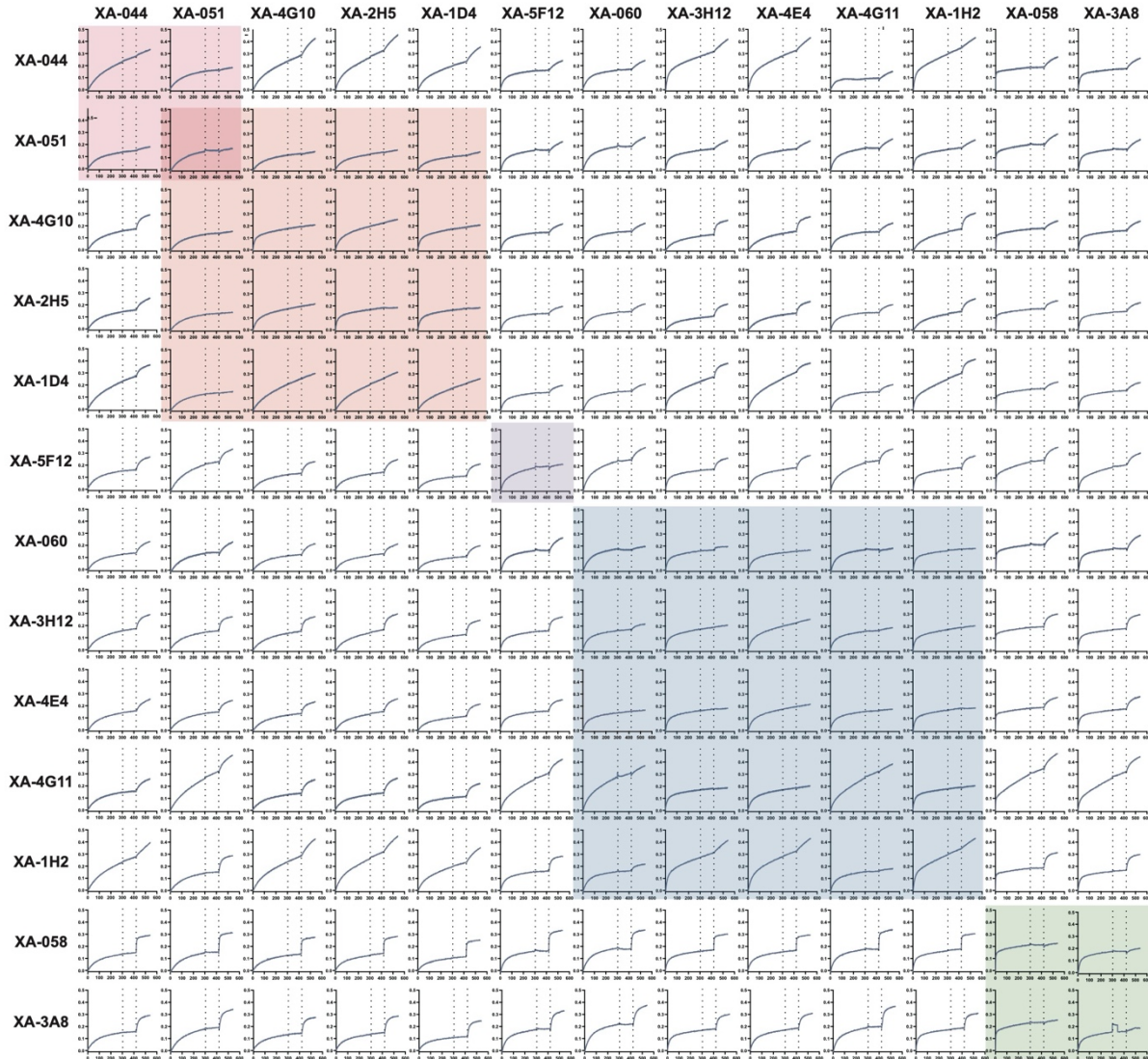
120 **Extended Data Fig. 2 | Characterization of isolated neutralizing antibodies.**

121 **a**, Immunogenetic features of 15 antigen-specific BCR sequences isolated from HFERS convalescent do-
122 nors, including donor origin, heavy- and light-chain CDR3 amino acid sequences and lengths, somatic
123 hypermutation frequencies, and V/J-gene usage and alleles.

124 **b,c**, Representative ELISA binding curves of isolated mAbs against recombinant Gn and Gc (**b**) or Gn^HGc
125 proteins (**c**). Data are mean \pm SEM from two independent experiments; corresponding EC₅₀ values are
126 summarized in Fig. 2c.

127 **d**, Representative neutralization curves of isolated mAbs against rVSV-HTNV-GFP, rVSV-SEOV-GFP,
128 rVSV-SNV-GFP, and rVSV-ANDV-GFP pseudoviruses. Data are mean \pm SEM from two independent ex-
129 periments; corresponding IC₅₀ values are summarized in Fig. 2d.

130 **e**, Representative immunofluorescence images showing neutralization of authentic HTNV. Vero E6 cells
131 were infected with HTNV (strain 76118) preincubated with neutralizing antibodies, and infection was
132 quantified by immunofluorescent staining of HTNV Nucleocapsid protein (NP).



133

134

Extended Data Fig. 3 | BLI-based epitope competition analysis of neutralizing antibodies. Recombi-

135

nant HTNV Gn^HGc protein was immobilized via binding to a primary neutralizing antibodies, followed

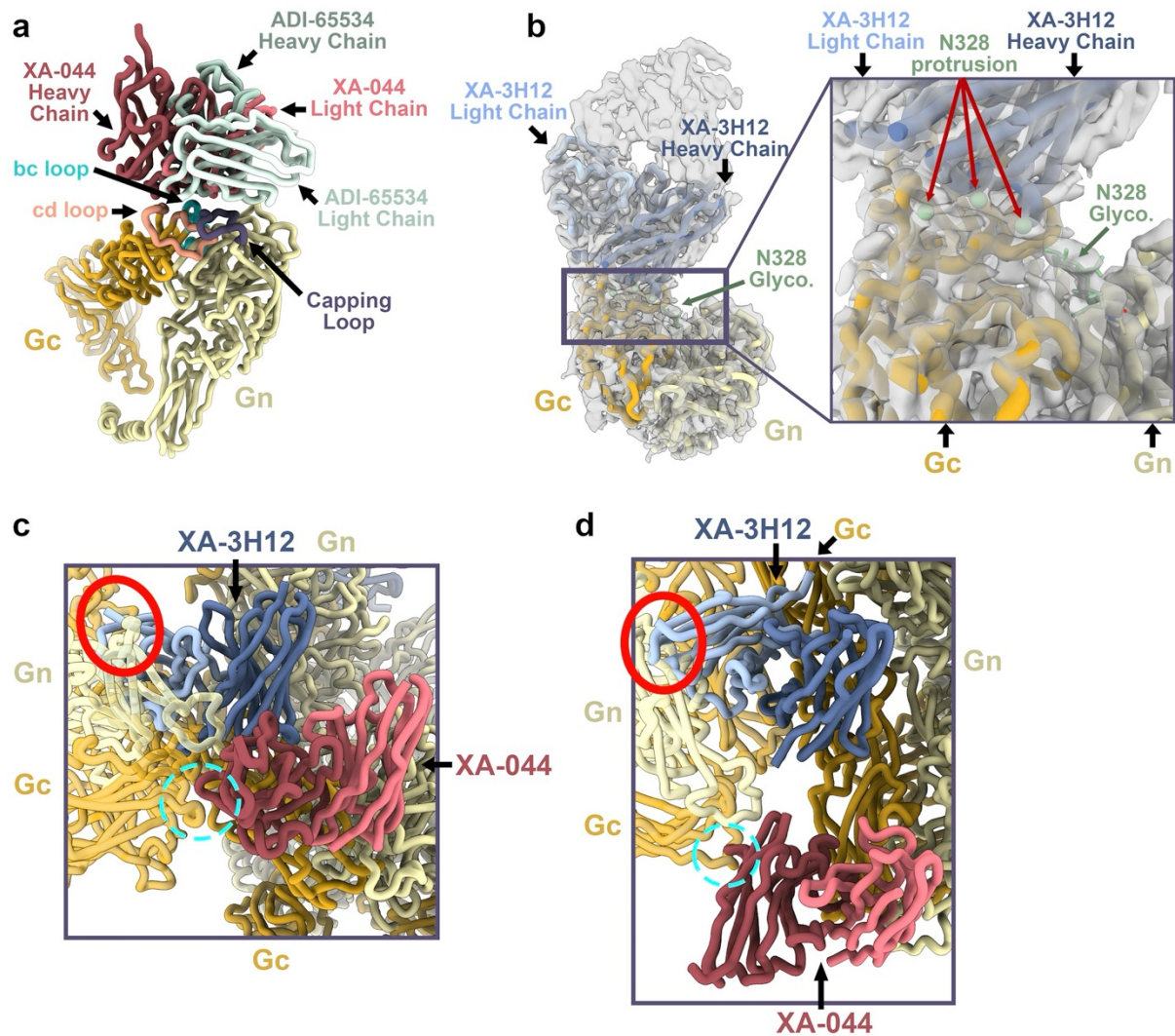
136

by binding assessment of a second neutralizing antibodies. Epitope competition was quantified as the dif-

137

ference in response (Δ RLU) between sequential antibody-binding steps. Related to Fig. 2e.

138



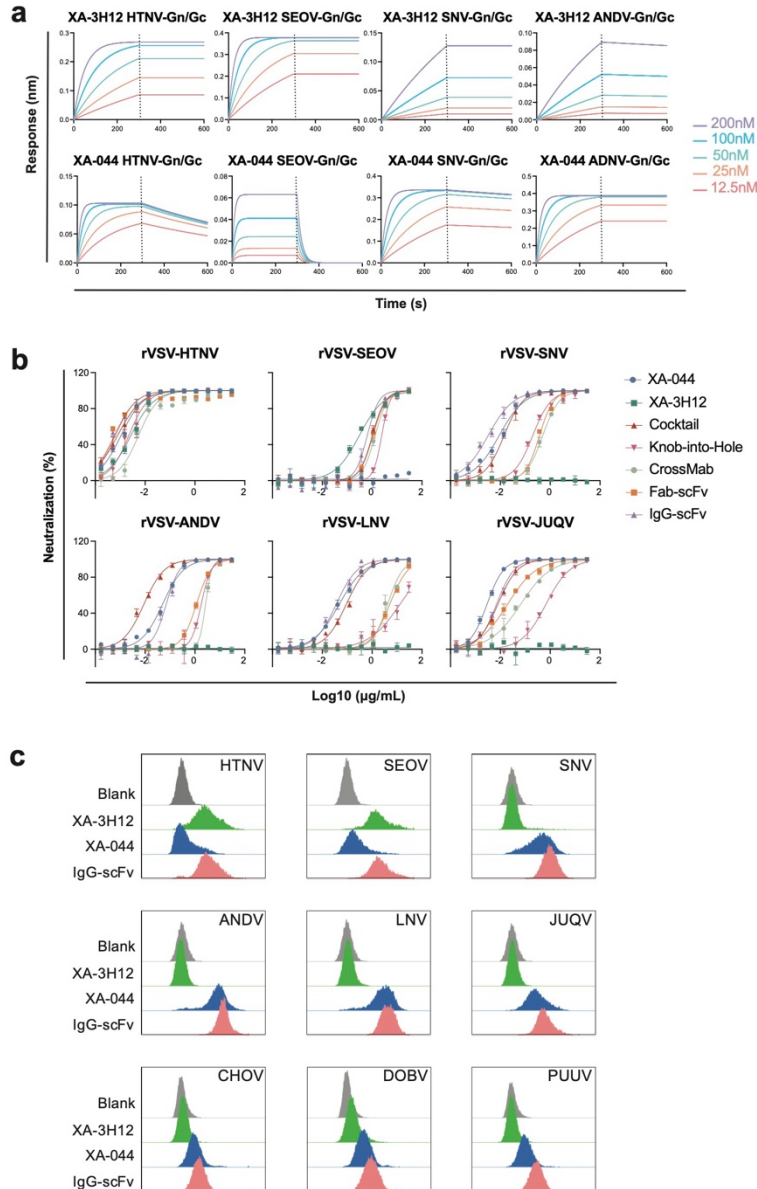
139

140 **Extended Data Fig. 4 | Focused analysis of XA-044 and XA-3H12 epitopes and neutralization mech-**
 141 **anism.**

142 **a**, Superposition of XA-044 on the ANDV Gn-Gc dimer bound by ADI-65534, showing overlapping
 143 epitopes with XA-044 shifted slightly toward the Gc fusion loops (bc and cd loops). Gn: yellow, Gc:
 144 gold; XA-044 heavy and light chains: dark and light red; ADI-65534 heavy and light chains: dark and
 145 light mint; Gc bc loop: cyan, Gc cd loop: salmon.

146 **b**, The N-glycan protruding from N328 of HTNV Gn interacts with the XA-044 heavy chain. Left, overall
 147 view; right, zoomed-in view with the XA-3H12 Fab-HTNV Gn^HGc complex fitted into the cryo-EM
 148 density map. The purple rectangle indicates the zoomed-in region. Built glycans are shown as green
 149 sticks, and hypothesized glycan protrusions are shown as green dots.

150 **c,d**, Zoomed-in views of steric clashes between XA-044 or XA-3H12 and a neighboring Gn-Gc tetramer
151 in the lattice, with XA-044 in red, XA-3H12 in blue, Gn in yellow, and Gc in gold. Cyan circles indicate a
152 potential minor clash between XA-044 and the neighboring tetramer, whereas red circles indicate major
153 clashes between XA-3H12 and the neighboring tetramer.
154



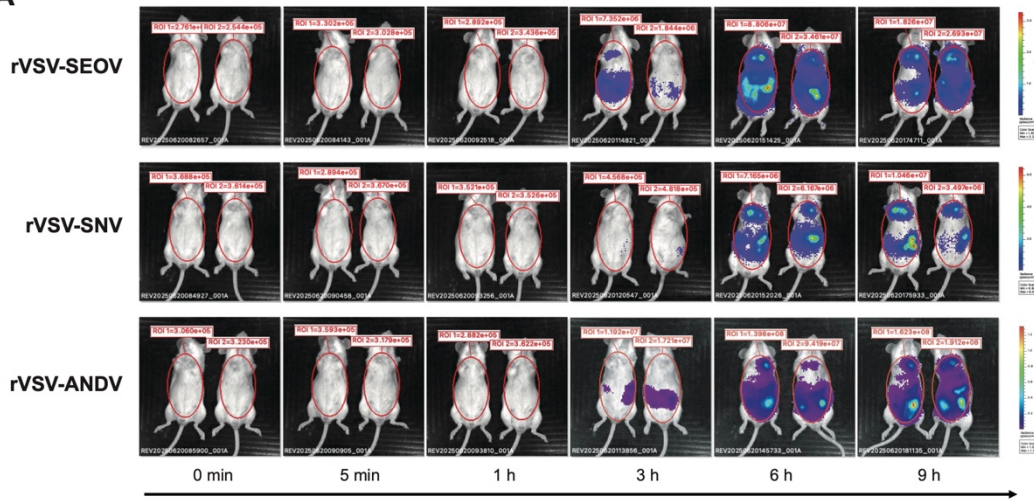
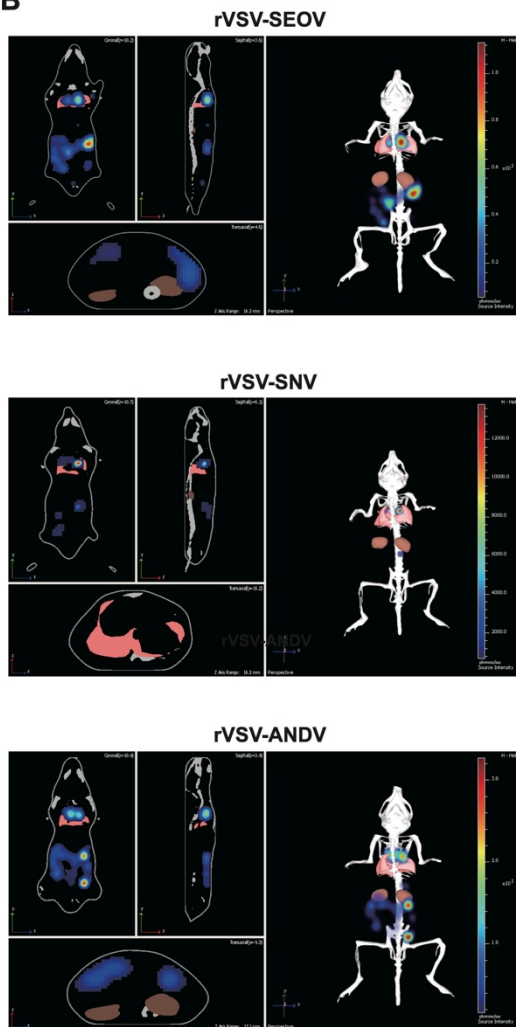
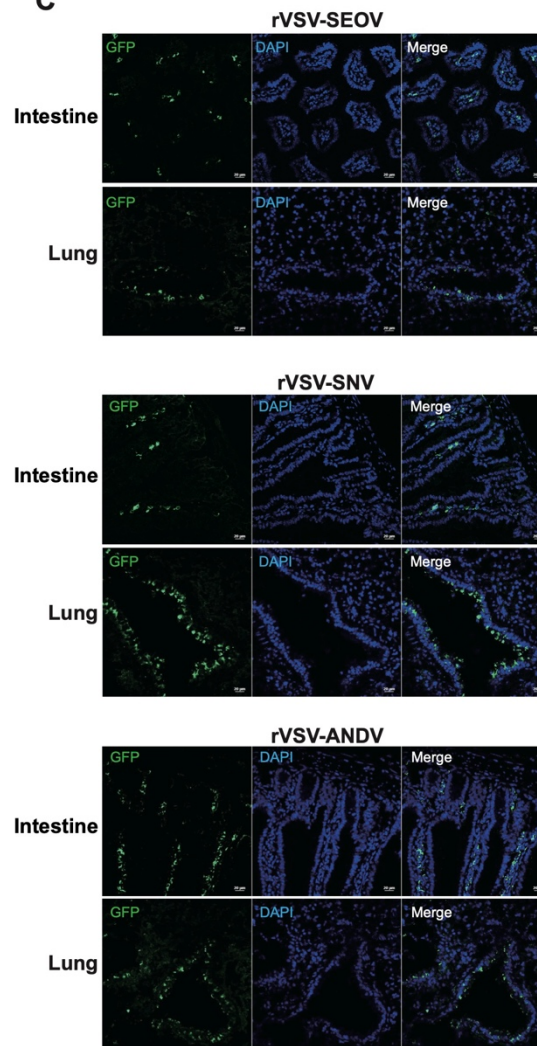
155

156 **Extended Data Fig. 5 | Characterization of selected NAb and bispecific antibodies.**

157 **a**, BLI analysis of NAb binding to HTNV-, SEOV-, SNV-, and ANDV-Gn^HGc. Binding kinetics were
 158 measured using 2-fold serial dilutions of recombinant Gn^HGc antigens (200-12.5 nM) and fit to a 1:1
 159 Langmuir model. Binding affinities are reported as K_D values.

160 **b**, Representative neutralization curves of parental NAbs, an antibody cocktail, and bispecific antibodies
 161 against hantavirus pseudoviruses, including rVSV- HTNV, rVSV- SEOV, rVSV- SNV, rVSV- ANDV, rVSV-
 162 JUQV, and rVSV- LNV. Data are mean \pm SEM from two independent experiments; corresponding IC_{50}
 163 values are summarized in Fig. 3d.

164 **c**, Flow cytometric analysis of antibody binding to full-length hantavirus glycoprotein (GP). HEK293T
165 cells expressing the indicated GP were incubated with individual antibodies followed by fluorophore-con-
166 jugated secondary antibody staining. Colored histograms indicate specific binding, and the gray histogram
167 indicates the negative control. Related to Figure 3f.
168

A**B****C**

170 **Extended Data Fig. 6 | Establishment of a pseudovirus-based *in vivo* infection system.**
171 **a,** Temporal dynamics of bioluminescence signals in rVSV-SEOV-Luc, rVSV-SNV-Luc, and rVSV-
172 ANDV-Luc infected mice. *In vivo* bioluminescence imaging was performed at the indicated time points
173 after inoculation. All images were processed and displayed using the same intensity scale.
174 **b,** Representative 3D images of mice inoculated with rVSV-SEOV-Luc, rVSV-SNV-Luc, or rVSV-
175 ANDV-Luc at 6 h post-inoculation.
176 **c,** Immunofluorescence analysis of rVSV-SEOV-GFP, rVSV-SNV-GFP, and rVSV-ANDV-GFP infec-
177 tion in the intestine (upper panels) and lung (lower panels) collected 6 h after inoculation. GFP-positive
178 signals are shown in green, and nuclei were counterstained with DAPI (blue). Scale bars, 75 μ m.
179

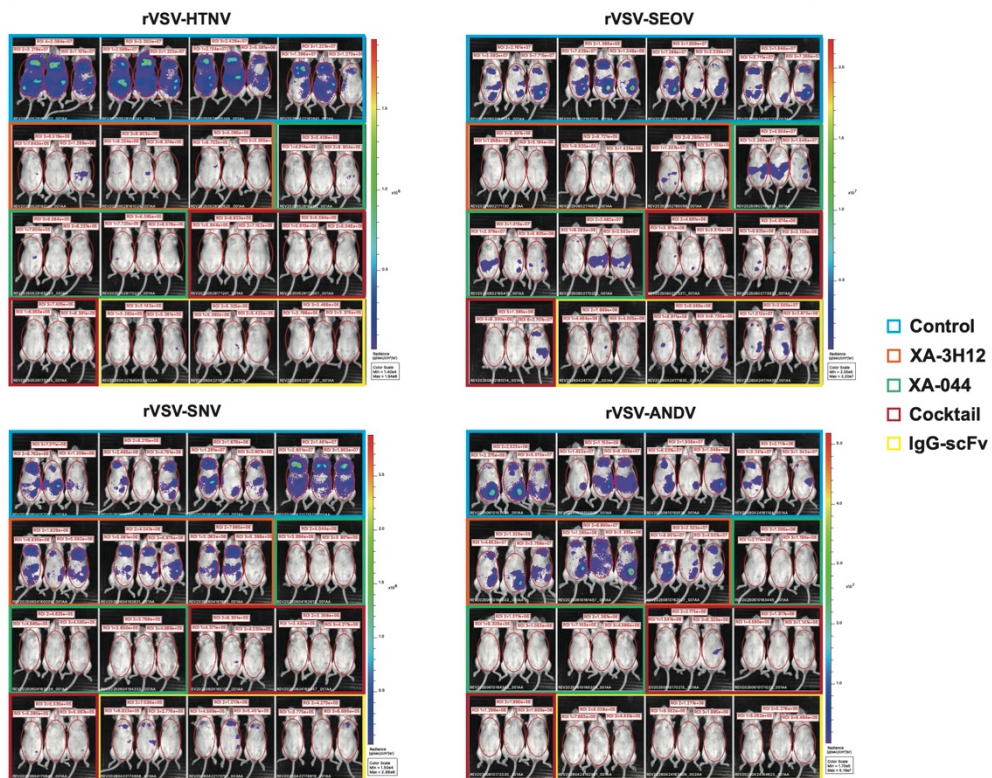
a

With incubation



b

Prophylaxis



181 **Extended Data Fig. 7 | Bioluminescence imaging related to Figures 4 and 5.**

182 **a**, Complete dataset for antibody-mediated blockade of pseudovirus entry shown in Fig. 4f-i.

183 **d**, Complete dataset for the prophylactic antibody protection study shown in Fig. 5b-e.

184

185

186 **Extended Data Table 1 | Immunogenetic analysis and experimental data of the hantavirus Gn/Gc-**
187 **specific antibodies.**

188

189 **Extended Data Table 2 | Cryo-EM data collection, processing and model refinement statistics.**

190